The Vertical Structure of Large-Scale Unsteady Currents

ANTOINE HOCHET, ALAIN COLIN DE VERDIÈRE, AND ROBERT SCOTT

Laboratoire de Physique des Océans, UMR6523 (CNRS, UBO, IFREMER, IRD), Brest, France

ABSTRACT

A linear model based on the quasigeostrophic equations is constructed in order to predict the vertical structure of Rossby waves and, more broadly, of anomalies resolved by altimeter data, roughly with periods longer than 20 days and with wavelengths larger than 100 km. The subsurface field is reconstructed from sea surface height and climatological stratification. The solution is calculated in periodic rectangular regions with a 3D discrete Fourier transform. The effect of the mean flow on Rossby waves is neglected, which the authors believe is a reasonable approximation for low latitudes. The method used has been tested with an idealized double-gyre simulation [performed with the Miami Isopycnal Coordinate Ocean Model (MICOM)]. The linear model is able to give reasonable predictions of subsurface currents at low latitudes (below approximately 30°) and for relatively weak mean flow. However, the predictions degrade with stronger mean flows and higher latitudes. The subsurface velocities calculated with this model using AVISO altimetric data and velocities from current meters have also been compared. Results show that the model gives reasonably accurate results away from the top and bottom boundaries, side boundaries, and far from western boundary currents. This study found, for the regions where the model is valid, an energy partition of the traditional modes of approximately 68% in the barotropic mode and 25% in the first baroclinic mode. Only 20% of the observed kinetic energy can be attributed to free Rossby waves of long periods that propagate energy to the west.

1. Introduction

Rossby waves play an important role in the spinup of the ocean and are its main response to changes in atmospheric forcing (Pedlosky 1987; Gill 1982; Anderson and Gill 1975). These waves are the way by which information is transmitted in the zonal direction. As a result, they set up the response time of the ocean to changes and are essential in understanding the climate system. For instance, in Jacobs et al. (1994), the authors suggested that an El Niño event forced a Rossby wave that, a decade later, influenced the Kuroshio position and then the weather pattern over North America.

Although surface characteristics of Rossby waves have been widely studied, thanks to advances in satellite observations, their vertical structure is poorly known. This is mostly due to the difficulties in getting observations at depth for waves with wavelength of several hundreds of kilometers and periods up to several years (Qiu and Chen 2005).

The theory for such waves is well known under the assumptions of a linear ocean at rest over a flat bottom (Gill 1982). This standard theory was, however, found to be unable to explain the observed propagation speed of surface sea level anomalies. Indeed, Chelton and Schlax (1996) used Hovmöller diagrams to show that the observed propagation speed for what was expected to be Rossby waves was faster than the first baroclinic long Rossby wave phase speed. This result was challenged by Zang and Wunsch (1999) who found, using a method that discriminates between wave constituents, that a substantial fraction of energy was consistent with standard theory. Osychny and Cornillon (2004) used a zonal fast Fourier transform (FFT) to compare the first baroclinic long Rossby wave dispersion relationship with observations for several latitudes in the North Atlantic and found that the observed phase speeds were larger than theory, with larger differences occurring at shorter periods. A step forward was made in Tulloch et al. (2009) who abandoned the long-wave approximation and chose the horizontal length scale of the

Corresponding author address: Antoine Hochet, LPO, Avenue le Gorgeu, 29200 Brest, France.
E-mail: antoine.hochet@univ-brest.fr

waves in order to fit the observed phase speed. It appears, from this set of studies, that at those frequencies and wavelengths, the signal is broadband and does not agree well with the linear theory of first baroclinic Rossby waves. Reasons for these discrepancies with theory, mean flow effect, topographic effects, and possible forcing action (the waves are not free) have been investigated in a number of studies (Killworth et al. 1997; Killworth and Blundell 1999, 2003a,b; Tailleux and McWilliams 2000, 2001; White 1977).

The goal of this article is to show that it is possible to "read" the vertical structure in the surface data. The main question that we are addressing is the following: given the sea surface height from altimetry (and thus the observed frequency wavenumber distribution) to what extent can the linear quasigeostrophic (QG) equations predict the vertical structure of the waves?

Wunsch (1997) found from current meter data (107 moorings inhomogeneously distributed over the World Ocean) that the daily mean currents were, on average, dominated by the barotropic and first baroclinic mode (unfortunately, no indication of the temporal or spatial variation about the mean was given). A second result from his study, which is widely used in the literature, is that altimeter data should predominantly reflect first baroclinic mode motions.

Recently, Scott and Furnival (2012) tested three strategies for extrapolating the surface geostrophic velocities below the surface: the first using only the barotropic or baroclinic mode, the second using a combination of both modes, and the third using a new set of functions. Even if their three strategies gave poor results below 800 m, they showed that the projection of the energy on each vertical mode changes a lot with time and space. Thus, we deduce that if one wants to extrapolate the surface signal downward, one would have to take this into account. Colin de Verdière and Tailleux (2005) showed that the influence of a mean flow on planetary Rossby waves is expected to be important only at high latitudes (between 30° and 50°) where the parameter $R^2 = (\beta N^2 h)/(f^2 U_z)$ (which is the ratio of β to its topographic equivalent induced by slopes $f U_z/N^2$ of the mean density surfaces) is intermediate $(1 < R^2 < 10)$. As a result, we expect the linear quasigeostrophic equations to be able to predict a correct vertical structure at low latitudes, where the mean flow does not have a significant influence on anomalies.

Lapeyre and Klein (2006) used quasigeostrophic dynamics combined with sea surface temperature (SST) data at the surface to invert potential vorticity and find the 3D geostrophic velocity field for the upper ocean. Their method, called eSQG, is claimed to work well for mesoscale dynamics, but, according to Isern-Fontanet et al. (2008), the success of the method depends greatly

on the quality of the SST that needs to be a good proxy of the density anomaly at the base of the mixed layer, and therefore SST is not always a good indicator of what happens below the surface. In contrast, sea surface height (SSH) from satellite altimetry cannot be influenced by a change of temperature in the thin mixed layer and thus is more able to reflect under surface dynamics. As a result, we choose in this study to only use SSH as the surface boundary condition. SSH has been used in several articles to give information about the subsurface flow. For example, in Hirschi et al. (2009) SSH is tested as an indicator for the variability of the Atlantic meridional mass transport; Lapeyre (2009) suggested that the sea surface height is dominated by a surface-trapped vertical mode rather than by the first baroclinic mode. Wang et al. (2013) improved the Lapeyre and Klein (2006) theory by reconstructing the subsurface large-scale flow with the SSH projected on the barotropic and first baroclinic mode using two conditions: SSH at the surface boundary and no bottom pressure anomalies.

The present work is organized as follows: we first construct a simple model based on the linear quasigeostrophic equations to predict the vertical structure of motions with frequencies and wavelengths within the range of Rossby waves (section 2). Next we investigate, with an idealized numerical model (section 3a), the different parameters (latitude and wind intensity) that influence the ability of this model to give accurate vertical structures. We then test the model with real data (section 3b) using AVISO (SSH) as the boundary condition and current meters to test our predictions. The final section summarizes and discusses the results.

2. Governing equations and analytical solutions

a. Equations

We are interested in long periods (>30 days) and large space scales (>100 km but smaller than 1000 km), which are well described by the quasigeostrophic equations. If lateral dissipation, bottom friction, buoyancy mixing, and external forcing are neglected, if we assume that the background buoyancy does not depend on horizontal space, and if we make the β-plane approximation, we obtain the equation for the conservation of potential vorticity:

$$\frac{D}{Dt}\left\{\nabla^2\psi + \beta y + \frac{\partial}{\partial z}\left[\frac{f_0^2}{N^2(z)}\frac{\partial\psi}{\partial z}\right]\right\} = 0, \qquad (1)$$

where ψ is the streamfunction; f_0 is the local Coriolis parameter; β is its linear variation coefficient; (x, y, z) are the zonal, meridional, and vertical directions, respectively; t is the time; N is the buoyancy frequency; and

$D/Dt(.) = \partial_t(.) + u\partial_x(.) + v\partial_y(.)$ with (u, v) as the zonal and meridional geostrophic velocities. The linear version of (1) will be used and is valid as long as $R_\beta = U/(\beta L^2) \ll 1$, where R_β is the vorticity Rossby number, U is the scale of the velocity, and L is the scale of the variation of U. For example, if $\beta = 1.0 \times 10^{-11}\,\mathrm{s}^{-1}\,\mathrm{m}^{-1}$, $U \sim 0.1\,\mathrm{m\,s}^{-1}$, then L should be larger than 100 km to make the vorticity Rossby number smaller than 1. To solve this equation, we need boundary conditions at the top and bottom. We choose to assume a flat bottom here for simplicity: $(\partial^2\psi)/(\partial z \partial t)(z = -H) = 0$, where H is the depth of the ocean (a constant). At the top we assume that we know the sea elevation $\eta(x, y, t)$ given by the altimetric SSH from which we infer $\psi(x, y, z = 0, t)$ with $\psi(x, y, z = 0, t) = (g/f_0)\eta(x, y, t)$.

To solve (1), it is customary in oceanography to first expand the solution in terms of vertical modes and then solve the equation for the horizontal structure of each mode. Philander (1978) emphasized that one may alternatively choose to expand the solution in terms of horizontal modes and then solve an equation for the vertical structure of the flow. As there is no lid at the top of the atmosphere, vertical modes do not exist and this second approach has been widely used to compute the stratospheric response to forcing by tropospheric disturbances below [see review by Andrews et al. (1987)]. This approach has motivated the present paper in which we compute how the SSH anomalies are linked to the deep oceanic motion. We do not consider here the lateral boundary conditions that the horizontal modes must satisfy at coastlines essentially because many of our assumptions (weakness of mean flows and linearity) are not valid in the western boundary current regions. We develop here the theory for the ocean interior away from boundaries, an assumption that allows us to use at first a simple Fourier decomposition in the zonal and meridional directions. Assuming therefore that the horizontal boundaries of the domain of SSH observations are periodic, we can decompose the SSH in a three-dimensional Fourier series:

$$\eta(x, y, t) = \sum_{(k,l,\omega)} \alpha_{(k,l,\omega)} \exp[i(kx + ly + \omega t)], \quad (2)$$

where (k, l, ω) are the zonal and meridional wavelengths and frequencies, and $\alpha_{(k,l,\omega)}$ is the Fourier coefficient associated with (k, l, ω). We then look for ψ under the following form:

$$\psi(x, y, z, t) = \sum_{(k,l,\omega)} F(z)_{(k,l,\omega)} \exp[i(kx + ly + \omega t)]. \quad (3)$$

And using the linear version of (1) and (3) and boundary conditions at the top and bottom, we obtain the following system:
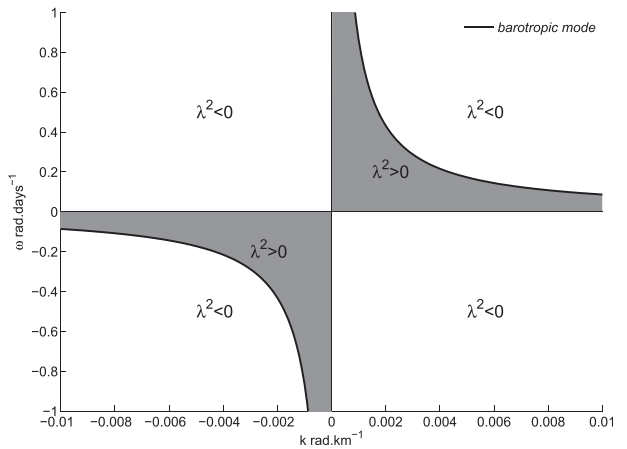

FIG. 1. In black and white, respectively, the two zones (for the meridional wavenumber $l = 0$) for which $\lambda^2 > 0$ and $\lambda^2 < 0$. Black line is the barotropic mode dispersion relationship.

$$\begin{cases} F(z = 0) = \dfrac{g}{f_0}\alpha_{(k,l,\omega)} \\[2mm] \dfrac{d}{dz}\left[\dfrac{f_0^2}{N^2(z)}\dfrac{dF}{dz}\right] + \lambda^2 F(z) = 0\,, \\[2mm] \dfrac{dF}{dz}(z = -H) = 0 \end{cases} \quad (4)$$

where $\lambda^2 = -(k^2 + l^2) + \beta(k/\omega)$. The qualitative nature of the solution depends upon the sign of λ^2. Let us assume that N is constant. If $\lambda^2 < 0$, then F will be exponential, trapped at the surface, whereas if $\lambda^2 > 0$, F will oscillate. Let us examine λ^2 and for the sake of simplicity assume $l = 0$. Imagine that a wave is propagating zonally with a phase velocity c: with $\omega = -kc$, the wave is going westward if $c < 0$ and eastward if $c > 0$. We can write $\lambda^2 = -k^2 - (\beta/c)$. If the wave goes eastward, it is trapped at the surface (since $\lambda^2 < 0$), whereas if it goes westward, it is trapped at the surface only if $|c| > \beta/k^2$ and has an oscillating structure otherwise. To summarize, only westward-propagating waves with a sufficiently small phase velocity will have an oscillating vertical structure and this regime is that of free waves. Figure 1 shows, in the Fourier space, the variation of the sign of λ^2 with k and ω, the zonal wavelength and the frequency (l, the meridional wavelength, is zero).

b. Analytical solution with a constant buoyancy frequency

The solution for N constant is certainly not realistic but is useful to understand the system [(4)]. The solution is as follows: for $\lambda^2 < 0$, set $\mu^2 = -\lambda^2$, where

$$F(z) = \frac{g}{f_0}\alpha_{(k,l,\omega)}\left[\cosh\left(\frac{N}{f_0}\mu z\right) \\ + \tanh\left(\frac{N}{f_0}\mu H\right)\sinh\left(\frac{N}{f_0}\mu z\right)\right], \qquad (5)$$

and for $\lambda^2 > 0$,

$$F(z) = \frac{g}{f_0}\alpha_{(k,l,\omega)}\left[\cos\left(\frac{N}{f_0}\lambda z\right) - \tan\left(\frac{N}{f_0}\lambda H\right)\sin\left(\frac{N}{f_0}\lambda z\right)\right]. \qquad (6)$$

When $\lambda^2 > 0$, and where $(N/f_0)\lambda H = \pi/2, 3\pi/2\ldots$, (4) does not have a solution. The surface data excite resonantly free modes satisfying $\psi = 0$ at the surface and $\partial_z\psi = 0$ at the bottom. The vertical velocity of these modes does not vanish at the surface as it should under the rigid-lid approximation $[(N^2 H)/g \ll 1]$. Since the rigid lid is a good approximation for the time scales and space scales under consideration, the vertical velocity w at the surface must be created by external forcing, for example, wind through Ekman pumping. Thus, a very large vertical velocity is in fact an unrealistic forcing. This can be interpreted in two different ways: first, a given forcing at (k, l, ω) creates a SSH amplitude $|\hat{\eta}(k, l, \omega)|$ that is zero near $(N/f_0)\lambda H = \pi/2, 3\pi/2\ldots$ and that is largest close to the dispersion relationships. Second, the forcing becomes unrealistic for frequencies and wavelengths close to $(N/f_0)\lambda H = \pi/2, 3\pi/2\ldots$ for a given SSH amplitude $|\hat{\eta}(k, l, \omega)|$. We deduce from this that if forced waves can be seen in the altimetry in the $\lambda^2 > 0$ regime, they must lie near the dispersion relationship of the free modes, at least when our assumptions are valid.

The principal difficulty of the present method is to find ways to remove the resonance of these spurious modes that appear where $\lambda^2 > 0$. Traditionally dissipation or transient effects as in Matsuno (1970) are added to remove singularities at resonances, but these methods were not found satisfactory. A filter to remove the energy near the spurious modes has been tested but turned out to filter a very large percentage of the energy in $\lambda^2 > 0$ (typically more than 70%). Indeed, as noted by Zang and Wunsch (1999), a large part of the energy lies far from the dispersion relationship of Rossby waves, where our linear model gives a resonant response. We also tested Ekman-type bottom friction and lateral viscous dissipation (which are an indirect way of filtering the data), but the results were not found satisfactory either.

Finally, our method consists in keeping the boundary condition $\partial\psi/\partial z(z = -H) = 0$, where $\lambda^2 < 0$, and use $\partial\psi/\partial z(z = 0) = 0$, where $\lambda^2 > 0$. For $\lambda^2 > 0$, the solution (6) becomes

$$F(z) = \frac{g}{f_0}\alpha_{(k,l,\omega)}\cos\left(\frac{N}{f_0}\lambda z\right), \qquad (7)$$

and the resonant modes are removed. This method is comparable to the atmospheric case depicted above. The condition $\partial\psi/\partial z(z = 0) = 0$ imposes zero density anomalies at the surface and assumes therefore that the SSH variability is not directly forced when $\lambda^2 > 0$. At the bottom ($z = -H$) the vertical velocity is now different from zero except for the traditional vertical modes for which $(N/f_0)\lambda H \equiv \pi, 2\pi, 3\pi\ldots$. The vertical velocity at the bottom is

$$w_{\text{bottom}} = -\frac{f_0}{N_0^2}\omega\frac{dF}{dz}(z = -H) \\ = -\frac{g}{f_0}\alpha_{(k,l,\omega)}\frac{\omega}{N_0}\lambda\sin\left(\frac{N_0}{f_0}\lambda H\right).$$

Given the time scales, space scales, and latitudes under consideration, the most likely explanation is a nonzero topography for which the vertical velocity is given by $w = \mathbf{J}[\psi, \text{topo}(x, y)]$, where $\text{topo}(x, y)$ is the topography. Thus, all the $\lambda^2 > 0$ energy that is not situated on the dispersion relation of the traditional modes (for which $\partial\psi/\partial z = 0$ at the bottom) is explained in our model as unforced modes modified by the topography.

For $\lambda^2 < 0$, we keep the no vertical velocity condition at the bottom, $\partial\psi/\partial z(z = -H) = 0$, to filter out the bottom-trapped Rossby waves that cannot be observed in the altimetry. The density anomalies are thus allowed at the surface since $\partial\psi/\partial z(z = 0) \neq 0$. This surface condition seems to be important to reconstruct the subsurface field outside the free Rossby wave regime (see, e.g., Lapeyre and Klein 2006). Moreover, using the condition $\partial\psi/\partial z(z = 0) = 0$ for the $\lambda^2 < 0$ case would lead to very large pressure anomalies at depth. For example, when the buoyancy frequency is a constant, with no density anomalies at the surface, the solution is $F(z) = (g/f_0)\alpha_{(k,l,\omega)}\cosh[(N/f_0)\lambda z]$ and becomes very large near the bottom. When $\lambda^2 \ll 0$, the solution given by (5) becomes very close to the linear surface quasigeostrophic (SQG) solution: the surface-trapped mode $\exp[(k^2 + l^2)z]$ (see, e.g., Lapeyre 2009).

To sum up, when $\lambda^2 > 0$, the vertical structure is calculated with the following boundary conditions: $\psi(x, y, z = 0, t) = (g/f_0)\eta(x, y, t)$ and $\partial\psi/\partial z(z = 0) = 0$. The energy found outside the traditional dispersion relation is interpreted as free waves modified by the topography. When $\lambda^2 < 0$, the vertical structure is calculated with the following boundary conditions: $\psi(x, y, z = 0, t) = (g/f_0)\eta(x, y, t)$ and $\partial\psi/\partial z(z = -H) = 0$. The energy found in this regime is interpreted as forced motion.

Traditional vertical modes obtained by assuming $\partial_z \psi = 0$ at the surface and at the bottom are

$$\phi_n(z) = \cos\left(\frac{n\pi z}{H}\right), \tag{8}$$

where $n \in 0, 1, 2\ldots$ designates the number of the mode. The mode $n = 0$ is called the barotropic mode and n is the nth baroclinic mode. Project (7) on this set of vertical modes [(8)] to get for $\lambda(N/f_0) \neq (n\pi)/H$,

$$\begin{aligned}
\gamma_n &= \frac{2}{H} \int_{-H}^{0} F(z) \cos\left(\frac{n\pi z}{H}\right) dz \\
&= \frac{g}{f_0} \alpha_{(k,l,\omega)} (-1)^n \frac{2\frac{N}{f_0}\lambda H \sin\left(\frac{N}{f_0}\lambda H\right)}{\left(\frac{N}{f_0}\lambda H\right)^2 - (n\pi)^2},
\end{aligned} \tag{9}$$

and for $\lambda(N/f_0) = (n\pi)/H$,

$$\gamma_n = \frac{g}{f_0} \alpha_{(k,l,\omega)}, \tag{10}$$

where γ_n is the projection of F on the nth mode ϕ_n. The percentage of the vertical structure in each vertical mode is $|\gamma_n|/\sum_{n=0}^{\infty}|\gamma_n|$, and the maximum is reached when $\lambda(N/f_0) = (n\pi)/H$. This describes the idea that the closer the point (k, l, ω) from the dispersion relation of mode n, the closer its vertical structure will be from mode n. Imagine that we observe in the SSH data an anomaly with wavelength and frequency (k_0, l_0, ω_0). As the signal is broadband, it can be expected that $\forall j \in 0, 1, 2\ldots$, $\omega_0 \neq (\beta k_0)/(k_0^2 + l_0^2 + a_j^{-2})$ (a_j is the Rossby Radius for mode number j). In that case, our model will give a vertical structure that will be a superposition of the vertical structures of several traditional vertical modes. This vertical structure will depend upon the relative distance of (k_0, l_0, ω_0) from the curves $\omega_j = (\beta k)/(k^2 + l^2 + a_i^{-2})$.

c. A multilayered ocean

To consider a more realistic stratification, a layered model is constructed with the ideas described above.

The quasigeostrophic equations in a layered model give vorticity in layer j,

$$q_j = \nabla^2 \psi_j + \frac{f_0^2}{H_j}\left(\frac{\psi_{j-1} - \psi_j}{g'_{j-1}} - \frac{\psi_j - \psi_{j+1}}{g'_j}\right), \tag{11}$$

in the top layer 1,

$$q_1 = \nabla^2 \psi_1 + \frac{f_0^2}{H_1}\left(\frac{\psi_2 - \psi_1}{g'_1}\right), \tag{12}$$

and in the deepest layer M,

$$q_M = \nabla^2 \psi_M + \frac{f_0^2}{H_M}\left(\frac{\psi_{M-1} - \psi_M}{g'_{M-1}}\right), \tag{13}$$

where $H_1, H_2, \ldots H_M$ are the thickness of each layer, and $g'_j = g(\Delta\rho_j/\rho_0)$ with $\Delta\rho_j$ the density difference between layer j and $j + 1$. For each layer, the linear quasigeostrophic equations in layer j give

$$\frac{\partial q_j}{\partial t} + \beta \frac{\partial \psi_j}{\partial x} = 0, \tag{14}$$

in the top layer 1 the equations give

$$\frac{\partial q_1}{\partial t} + \beta \frac{\partial \psi_1}{\partial x} - \frac{f_0}{H_1} w_{\text{top}} = 0, \tag{15}$$

and in the deepest layer M they give

$$\frac{\partial q_M}{\partial t} + \beta \frac{\partial \psi_M}{\partial x} + \frac{f_0}{H_M} w_{\text{bottom}} = 0, \tag{16}$$

where w_{top} and w_{bottom} are the vertical velocities at the surface and bottom boundaries. As explained in the previous section, we will assume $w_{\text{top}} = 0$ when $\lambda^2 > 0$ and $w_{\text{bottom}} = 0$ when $\lambda^2 < 0$. We know ψ_1, and we want ψ_j, $j \in [\![2, M]\!]$. To do this, we write (as before) $\psi_j(x, y, t) = \sum_{(k,l,\omega)} \alpha_{(k,l,\omega)}^j \exp[i(kx + ly + \omega t)]$, and, using (11), (12), and (13) and (14), (15), and (16), we get the following system for α^i and w_{bottom} or w_{top}:

$$\begin{cases}
\left(-K^2 - \dfrac{f_0^2}{H_1 g'_1} + \dfrac{k\beta}{\omega}\right)\alpha^1 + \dfrac{f_0^2}{H_1 g'_1}\alpha^2 - \dfrac{f_0}{H_1} w_{\text{top}} = 0 \\[2ex]
\dfrac{f_0^2}{H_j g'_{j-1}}\alpha^{j-1} + \left[-K^2 - \dfrac{f_0^2}{H_j}\left(\dfrac{1}{g'_{j-1}} + \dfrac{1}{g'_j}\right) + \dfrac{k\beta}{\omega}\right]\alpha^j + \dfrac{f_0^2}{H_j g'_j}\alpha^{j+1} = 0, \quad j \in \{2, 3, \ldots, N-1\}, \\[2ex]
\dfrac{f_0^2}{H_M g'_{M-1}}\alpha^{M-1} + \left(-K^2 - \dfrac{f_0^2}{H_M g'_{M-1}} + \dfrac{k\beta}{\omega}\right)\alpha^M + \dfrac{f_0}{H_M} w_{\text{bottom}} = 0
\end{cases} \tag{17}$$

where $K^2 = k^2 + l^2$.

We thus have a system with M equations with M unknowns, among them is w_{top} or w_{bottom}, depending on the sign of λ^2. When $\lambda^2 > 0$, we impose w_{top} and solve system (17). As w_{bottom} is only in the last equation, the first $M - 1$ equations of the system can be solved independently of the last. When the values of α_i and $i \in [\![1, M]\!]$ are known, the last equation is used to get w_{bottom}. Similarly, when $\lambda^2 < 0$, we impose w_{bottom} and first solve the last $M - 1$ equations. Then, w_{top} is inferred from the first equation. Letting $H_i \to 0$ for each layer in (17), we recover system (4) showing that we are using the proper discretization. To easily understand how we proceed, we are going to present the calculation in the simple two-layer case.

d. Example: The two-layer model

In the layered case, there is an upper limit for the $\lambda^2 > 0$ case (where the top vertical velocity is set to zero) that is given by the highest baroclinic mode. Thus, we set the top vertical velocity to zero when $0 < \lambda^2 < \lambda^2_{\text{highest}}$, where $\lambda^2_{\text{highest}}$ is the squared inverse of the highest baroclinic mode deformation radius. The analogy with the continuous case can be understood easily knowing that in the continuous case there is an infinite set of modes with the deformation radius decreasing toward 0 and as a result making $\lambda^2_{\text{highest}}$ tend toward infinity. In the case of a two-layer model, we set $w_{\text{top}} = 0$ if $0 < \lambda^2 < (f_0^2/g_1')(1/H_1 + 1/H_2)$ and $w_{\text{bottom}} = 0$ otherwise. In the case $0 < \lambda^2 < (f_0^2/g_1')(1/H_1 + 1/H_2)$, we obtain α^2 with the equation

$$\alpha^2 = -\frac{H_1 g_1'}{f_0^2}\left(-K^2 - \frac{f_0^2}{H_1 g_1'} + \frac{k\beta}{\omega}\right)\alpha^1 \qquad (18)$$

and w_{bottom} with

$$w_{\text{bottom}} = -\frac{H_2}{f_0}\left[\frac{f_0^2}{H_2 g_1'}\alpha^1 + \left(-K^2 - \frac{f_0^2}{H_2 g_1'} + \frac{k\beta}{\omega}\right)\alpha^2\right].$$

$$(19)$$

Otherwise,

$$\alpha^2 = -\frac{H_2 g_1'}{f_0^2}\frac{\alpha^1}{-K^2 - \dfrac{f_0^2}{H_2 g_1'} + \dfrac{k\beta}{\omega}}, \qquad (20)$$

and

$$w_{\text{top}} = \frac{H_1}{f_0}\left[\frac{f_0^2}{H_1 g_1'}\alpha^2 + \left(-K^2 - \frac{f_0^2}{H_1 g_1'} + \frac{k\beta}{\omega}\right)\alpha^1\right]. \qquad (21)$$

TABLE 1. MICOM simulations used to assess the model. N_t is the number of days of integration after the spinup time. Parameters that do not change are resolution $\Delta X = 20$ km, depth (m) of the five layers $(H1, H2, H3, H4, H5) = (300, 400, 600, 800, 1900)$, $f_0 = 6 \times 10^{-5}$ s^{-1}, $\beta = 2 \times 10^{-11}$ s^{-1}, $N_x = 200$, Spin up = 5000 days, $N_t = 3000$ days.

Simulation	τ_x	N_y
1	0.01	200
2	0.02	200
3	0.03	200
4	0.04	200
5	0.05	200
6	0.06	200
7	0.07	200
8	0.08	200
9	0.09	200
10	0.10	200
11	0.05	300

3. Assessment of the method

a. Use of an idealized shallow-water model (MICOM) to assess the theoretical model and to study influences of latitudes and wind intensity

1) METHOD

To assess the linear model described in the previous section, we use an idealized shallow-water simulation performed with the Miami Isopycnal Coordinate Ocean Model (MICOM; Bleck and Boudra 1986). Inspired by the article of Holland and Rhines (1980), we simulate a double gyre, forced by a zonal wind stress $\tau_x(y) = \tau_x \cos(2\pi y/L_y)$, where τ_x is its amplitude, L_y is the basin meridional width, and y is the latitude. The model configuration has the following properties: bottom friction, five layers with $(H1, H2, H3, H4, H5) = (300, 400, 600, 800, 1900)$ meters, grid resolution $\Delta X = 20$ km, spinup time of 5000 days, and a square basin of 4000×4000 km is used in the 10 first simulations of Table 1, whereas the last simulation has a basin size of 4000×6000 km. Model output consists of 7-day averages. In Fig. 2, the temporal mean of ψ is shown in the first layer; two gyres are formed with a central jet toward the east. In the side panel of Fig. 2, the meridional variation of the wind stress is shown.

Anomalies in SSH occur through the forcing of Rossby waves by Kelvin waves on the eastern border, more information about this process can be found, for example, in Grimshaw and Allen (1988). Kelvin waves are forced in the western boundary layer through interaction between the western boundary and eddies. Milliff and McWilliams (1994) studied the interaction of a vortex with the western boundary of a closed ocean basin and showed that Kelvin waves are created by this
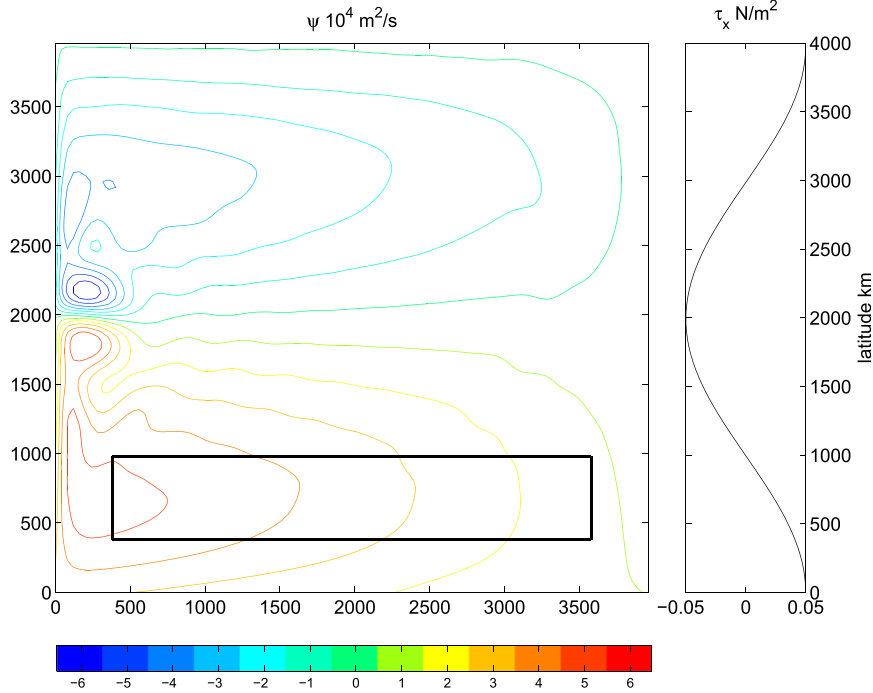
FIG. 2. (left) Contours of the temporal mean of ψ at the surface for simulation 5 ($\tau_x = 0.05\,\mathrm{N\,m^{-2}}$). Positive (negative) values denote a clockwise (anticlockwise) circulation. The black rectangle shows an example of the zone in which we perform the calculation of the vertical structure. (right) Zonal wind stress ($\mathrm{N\,m^{-2}}$) as a function of latitude.

interaction. In our double-gyre simulations, the Kelvin waves created at the western boundary propagate with the coast on their right, first on the southern border and then on the eastern border. Interaction of Rossby waves with the western boundary might also be part of the process. In our simulations, the vertical structure of flow anomalies depends upon bottom friction, wind intensity, latitude, and mean flow. We have verified that the spinup of the simulations is sufficiently long to ensure a statistical steady state. We choose the drag coefficient for the bottom friction $r \sim 0.001$ in order to approximately obtain anomalies with an energy partition of 45%, 45%, and 10% in, respectively, the barotropic, first baroclinic, and remaining vertical modes (second, third, and fourth). This proportion is near the one found in real data from current meters (Wunsch 1997). We use several simulations for which we vary the wind intensity; the different simulations with their parameters are summarized in Table 1.

To apply our method, we first select a horizontal rectangular zone to extract SSH. The size of the zone is chosen to maximize the correlation between the model results and our reconstruction; it has to be large enough in order to capture all the wavenumbers that are needed by the model for the prediction but not too large to avoid wavenumbers that do not reflect the dynamic of the

studied zone. The meridional size has to be sufficiently small to ensure the validity of the β-plane approximation. We found that a zonal size of 3000 km and a meridional size of 1000 km maximize the correlation. Before performing the three-dimensional FFT of the SSH, temporal and spatial averages have to be removed. The latter is computed at each time step through a best-fit plane of SSH data over the selected area. For each frequency and wavelength contained in the signal we calculate its vertical structure, using the method described above. Then the signal is reconstructed in the physical space using the inverse three-dimensional FFT. Figure 3 shows the proportion of each mode in the vertical structure for the five-layer simulation. The proportion of mode n is the largest near the curve of the dispersion relation of mode n.

Results are then compared with model output, using the temporal correlation at each point of the selected zone.

2) RESULTS

To better understand how our method works, let us write:

$$\psi_1 = a_1\chi_0(\text{layer} = 1) + a_2\chi_1(\text{layer} = 1) + a_3\chi_2(\text{layer} = 1)$$
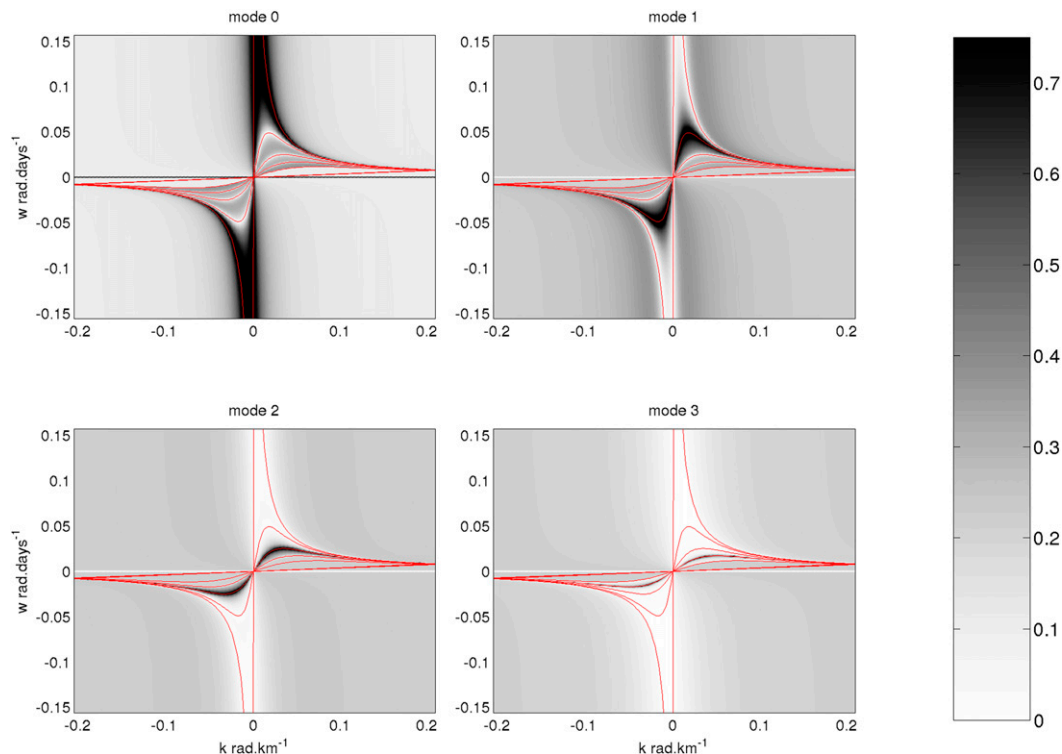$$+ a_4\chi_3(\text{layer} = 1) + a_5\chi_4(\text{layer} = 1),$$

$$(22)$$

FIG. 3. The variation of the percentage of energy in the four first vertical modes with the zonal wavelength and frequencies ($l = 0$ the meridional wavelength) for a five-layer ocean model. Dispersion relationships for the barotropic and four baroclinic modes are indicated by red curves.

where $(\chi_0, \ldots, \chi_4)$(layer = 1) are the traditional vertical modes evaluated at the surface, and $(a_1, a_2, a_3, a_4, a_4)$ is the projection of ψ on those modes. If we assume that, at the surface, most of the signal is in the first baroclinic mode, $\psi_1 = a_2 \chi_1$ [as often assumed in the literature, e.g., in Chelton and Schlax (1996)], then we find that the correlation between the prediction ψ/a_1 and the first baroclinic mode given by the numerical model output is very low: an average of 0.2. We find nothing here that tells, a priori, to which vertical mode ψ_1 most contributes. Moreover, ψ_1 could be a linear combination of several vertical modes. Different from many past studies, our method does not assume anything on the vertical structure associated with ψ_1. It calculates the coefficients $(a_1, a_2, a_3, a_4, a_5)$ according to the position of ψ_1 in the Fourier space as shown in Fig. 3: ψ_1 is mostly in χ_0 near the barotropic mode and mostly in χ_1 near the first baroclinic mode.

The vertical structure is first estimated for a relatively strong wind intensity (simulation 5, Table 1). We choose a zone in the southern gyre to assess the method where it is anticipated to give accurate predictions. Results are shown in Fig. 4. In the interior of the region, the correlation is always larger than 0.7, which means that the model effectively gives accurate results. As expected, the prediction is less accurate near the boundaries

because of our assumption of periodic boundary conditions. At the bottom of Fig. 4, we compare time series of data and prediction in the middle of the zone in order to confirm that the amplitudes are correct.

Figure 5 shows the temporal correlation between outputs and the prediction for the projection of ψ on the first baroclinic mode calculated with two different zones on outputs of simulation 11 (see Table 1). The first zone has a large meridional extent (3500 km), whereas the second one has a smaller meridional extent (1000 km) (see Fig. 5 for more details). The large zone shows accurate correlations (>0.6) around a latitude of 2000 km but low correlation (<0.5) in the northern and southern parts. The low correlations are because of the bad estimation of the Rossby wave's phase speed far from the central latitude (the QG equation assumes latitude-independent phase speed). The smaller zone is situated in the southern part of the large one and shows high correlation (>0.8) (however, low correlations are found in its southern part probably because of the influence of the basin southern boundary). Therefore, this figure first demonstrates the need to use a zone with a small meridional extent in order to compare the data with the correct phase speeds. Second, it shows that even for a relatively strong wind (here $\tau_x = 0.05$ N m^{-2}), the model is able to give accurate
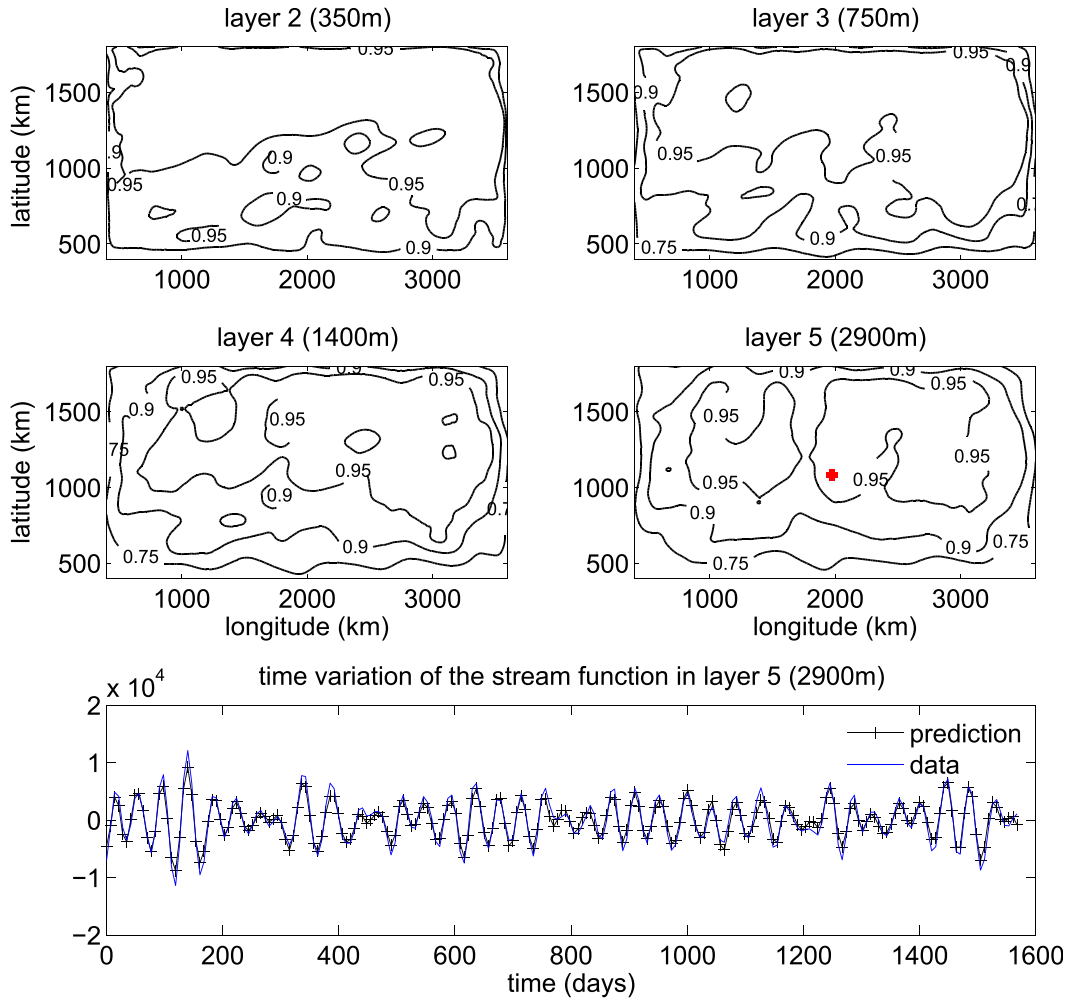
FIG. 4. Results of the comparison between our prediction and data from simulation number 5 [(1)]. (top) Temporal correlation for each layer below the first layer. (bottom) Comparison of time series for a virtual streamfunction meter ($m^2 s^{-1}$) situated in the middle of the last layer. The position of the streamfunction meter is indicated by a red cross.

predictions for the first baroclinic mode. In the next paragraph, we will investigate the influence of latitude and wind strength on the prediction.

3) LATITUDE EFFECT

The method works best when the vertical structure of the anomalies is in the lowest vertical modes. Indeed, low vertical modes propagate faster than high vertical modes and are, as a result, less influenced by non-linearities. By changing the latitude or the wind intensity in the simulations, we also change the proportion of SSH anomalies in each mode. So if we want to compare the influence of these parameters, we need to calculate correlations between model and simulation outputs for each vertical mode rather than for each layer.

We investigate the role of latitude on our prediction with simulation 11, which has a relatively strong wind

intensity ($\tau_x = 0.05\,\text{N m}^{-2}$) (see Table 1 for more details). This simulation has a large meridional extension (6000 km) that allows us to investigate the prediction on the southern gyre between 14° and 34° of latitude. The size of the analyzed zone is kept constant and it is moved meridionally to assess the results at each latitude. Figure 6 shows the spatial mean of the temporal correlation between prediction and output of the model. Recall that we saw in the last paragraph that the correlation is always small near the boundary. As a result, the spatial mean of the correlation will be lower than the correlation in the interior of the basin. The correlation for the first baroclinic mode decreases with latitude. The decrease of the first baroclinic mode can be explained as detailed below.

When latitude increases, the following occurs:

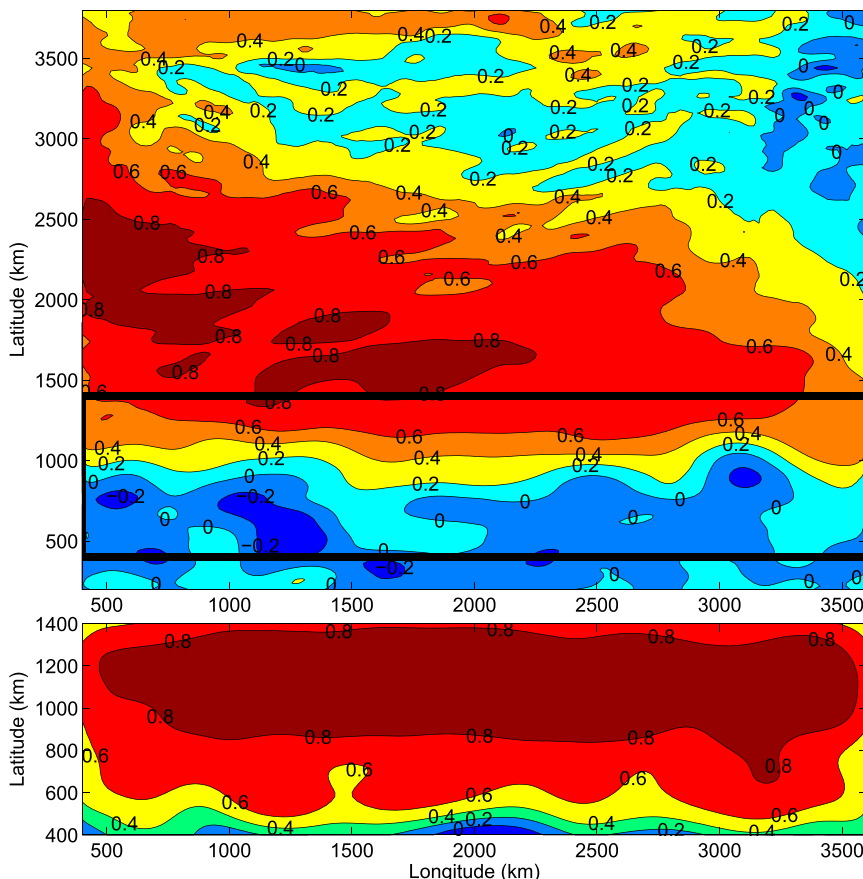(i) The phase speeds of baroclinic Rossby waves are slower and thus are more likely influenced by

FIG. 5. Results of the comparison between the projection of the streamfunction on the first baroclinic mode calculated from our prediction and calculated from simulation 5 outputs [(1)]. (top) Temporal correlation calculated in a large zone of 3500 km × 3200 km. (bottom) Temporal correlation calculated for a zone with a small latitudinal extent 1000 km × 3200 km. The rectangular zone used to calculate the correlation of the bottom figure is indicated by black lines in the top figure.

nonlinearities, $\epsilon = U/(\beta a^2)$ is the nondimensional number that controls the nonlinearities of the waves (*a* is deformation radius), βa^2 is of the order of the phase speed for a long baroclinic Rossby waves. Thus, ϵ is smaller for large phase speed (hence low latitude).

(ii) The mean flow is more likely to have an influence on anomalies; the nondimensional parameter that controls this effect is $R = (\beta N^2 h)/(f^2 U_z)$, which is the ratio of β to its topographic equivalent induced by the slopes fU_z/N^2 of the mean density surface (see Colin de Verdière and Tailleux 2005).

(iii) In the southern gyre of our simulation, the mean flow is larger in the middle of the basin where the western boundary currents extend in the basin interior. This is analogous to the situation in the Atlantic Ocean, when we study the gyre south of the Gulf Stream.

The barotropic mode correlation remains constant for latitudes lower than 30°N and decreases slowly afterward.

This can be explained by the fact that the phase speed of barotropic Rossby waves does not change significantly. For the second and higher baroclinic mode, we do not expect the model to give accurate predictions since those waves have very slow phase speeds and are thus more influenced by nonlinearities. A second reason for the low correlations of higher baroclinic mode is likely to be the relatively short time of integration (3000 days) of our model compared to the very long periods of those modes, for example, 300 days for the second baroclinic mode in the middle of the basin. This might lead to sampling problems.

4) WIND INTENSITY EFFECT

We now study the effect of the wind intensity on the ability of the model to predict the vertical structure. The position of the analyzed region is kept fixed, but we perform several simulations with different wind stress. The different parameters of the simulations (1 to 10) are
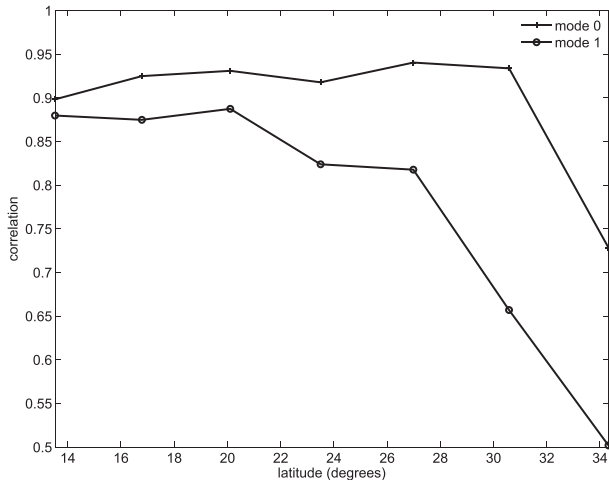
FIG. 6. Spatial mean of time correlation for different latitudes of the studied zone. The zonal and meridional sizes of the zone are constant: $1000 \, \text{km} \times 3000 \, \text{km}$. The two curves are the first two vertical modes, the cross is the barotropic mode, and the filled circle is the first baroclinic mode.

summarized in Table 1. The effects of an increase of the wind intensity are that

(i) the mean currents are stronger and thus increase their influence on anomalies; and

(ii) the intensity of anomalies increases and thus nonlinearities become larger.

Figure 7 shows the spatial mean of time correlations for an area of constant size for different wind intensities. The ability of the method to predict the vertical structure decreases with increasing wind intensity for the first baroclinic mode and remains almost constant for the barotropic mode.

To conclude this section, we have identified two parameters that can influence the ability of the prediction to reproduce the subsurface flow anomalies: the latitude and the wind intensity. The prediction gives better results for low latitude, less than 30° (N or S), and when the wind (and as a result nonlinearities and mean flow) is weak. In the ocean, geostrophic turbulence is concentrated near western boundary currents where the mean flow is also very strong. Thus, we cannot expect our method to give good predictions near these regions. However, below those regions, say south of 30° (or north in the Southern Hemisphere), the mean flow and turbulence are weaker and as a result the model will be able to give accurate results. Clearly, the linear quasigeostrophic assumptions behind our method are very idealized, and we are far from reproducing all the real ocean features such as the mixed layer, the topography, or the variable wind and buoyancy forcing. As a result, in the following section, we test our predictions against real data.
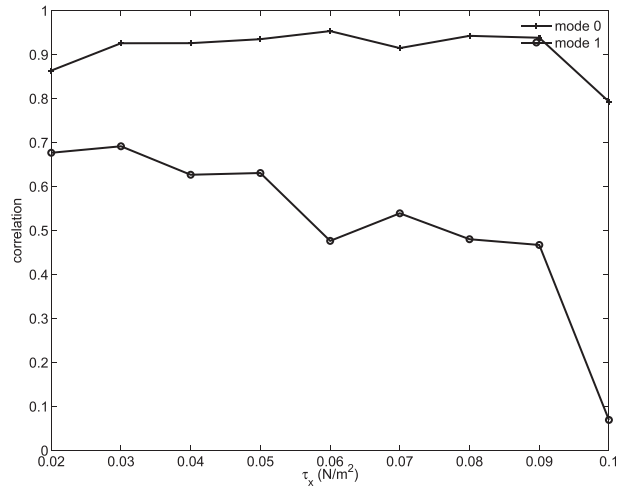

FIG. 7. As in Fig. 6, but for different wind intensities.

b. Use of altimetry data from AVISO and a mooring database to test the model

1) METHOD

To assess the method with real data, we use a current meter mooring database, collected from various institutions by D. Furnival and R. Scott [see Fig. 8 for the position of the mooring in the database that overlaps the AVISO era; more information about this database can be found in Wright et al. (2013)]; SSH measurements are obtained from AVISO and the *World Ocean Atlas* is used to compute N^2. The method used to perform the calculation of the vertical structure has a lot in common with that described in section 3a above. We begin by selecting a rectangular area for which we calculate the spatial mean of the Brunt–Väisälä frequency in order to obtain only a dependence on depth as required by QG assumptions. Then, we extract the SSH for the region. We first remove the time mean at each spatial point. Then the basin scale signal is removed by subtracting the best-fit 2D plane for each time step. We obtain $\psi(z = 0)$ by assuming geostrophy: $\psi(z = 0) = (g/f)\eta$. Three-dimensional FFT is applied before calculating the vertical structure using (4), and the signal is reconstructed in physical space with the inverse FFT. The vertical resolution is the same as that of N^2. To compare the calculation from our model with real data from current meters, we calculate $(u, v) = (-\partial\psi/\partial y, \partial\psi/\partial x)$. At this step, we can obtain the geostrophic velocity over the area defined earlier. Figure 9 shows a snapshot of the meridional velocity for a constant latitude (25°N) in zone 4 (see Fig. 8 to see the location of zone 4). At the surface, the velocity is given by the altimeter and below the surface by our prediction, which shows here a barotropic vertical structure at some places and a surface intensified structure at others.
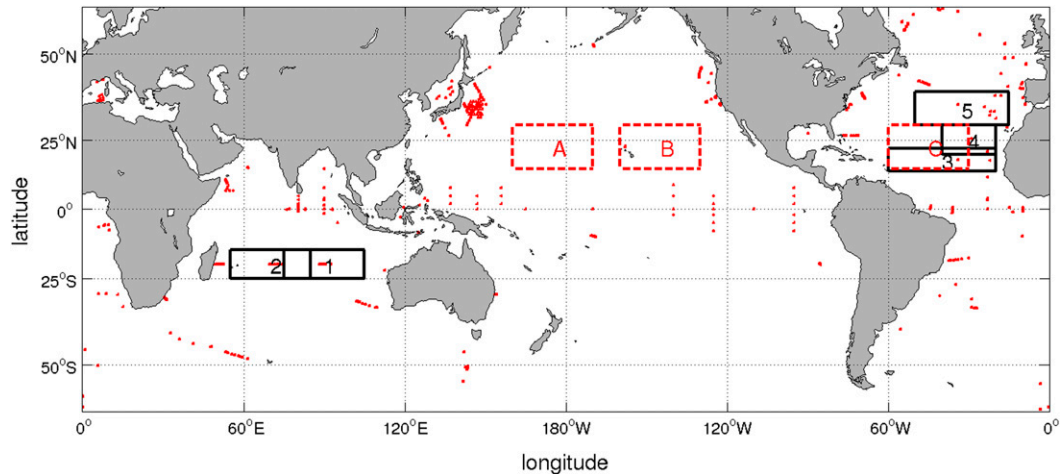
FIG. 8. Position of each mooring with records longer than 200 days in the database that intercept the dates of AVISO data, that is, after October 1992 (red dots). Black rectangle shows the position of the five different zones that we studied. Red rectangles A, B, and C are the positions at which the projection of the total energy on traditional vertical modes is calculated.

We now need to have the model outputs and the current meter measurements with the same grid. It is also necessary to low pass the data current meters since subinertial frequencies are assumed here.

We apply the following steps:

 (i) velocities u, v are interpolated from our model at the location of the current meters (longitude, latitude, and depth);
 (ii) we perform a day average of data and then remove the time mean. We then apply a low-pass filter to remove all periods shorter than 7 days and then interpolate onto the AVISO grid; and
(iii) once current meter data and predictions from our calculation are on the same grid, we apply a low-pass filter on both to remove all periods shorter than 20 days, and then the time mean is also removed.

We will use different strategies to compute the two datasets: calculating correlations and differences according to (23) and visual comparison of time series. Different regions of study are presented in Fig. 8, but we will only show here results for areas 4 and 5:

$$\mathrm{diff}(f_1, f_2) = \frac{\overline{[f_1(t) - f_2(t)]^2}}{\overline{f_1(t)^2 + f_2(t)^2}}, \qquad (23)$$

where f_1 and f_2 are the two variables for which we calculate the difference.

2) RESULTS

(i) Zone 4

This zone is situated in the Atlantic Ocean at a relatively low latitude (25°N) and in the east side of the basin
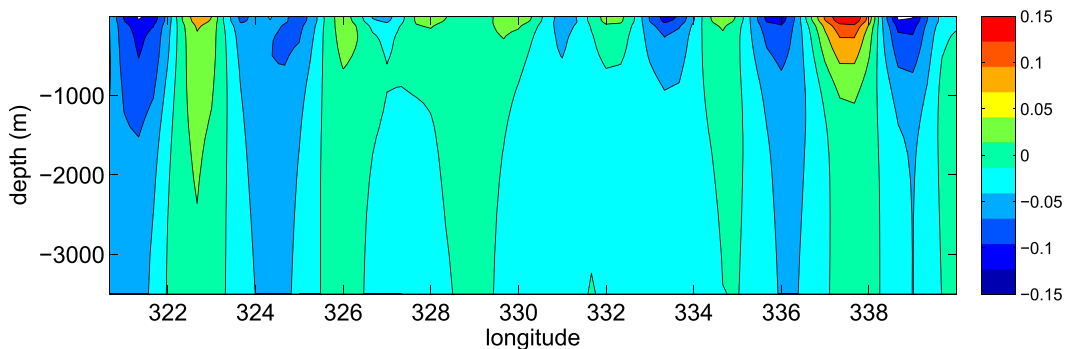

FIG. 9. Snapshot of the meridional velocity (m s^{-1}) calculated from a rectangle of SSH (zone 4; see Fig. 8) at latitude 25°N in the Atlantic Ocean.

Topography (meters) of Zone: 4

Mooring number 1; duration 244 days; number of Instruments: 12.

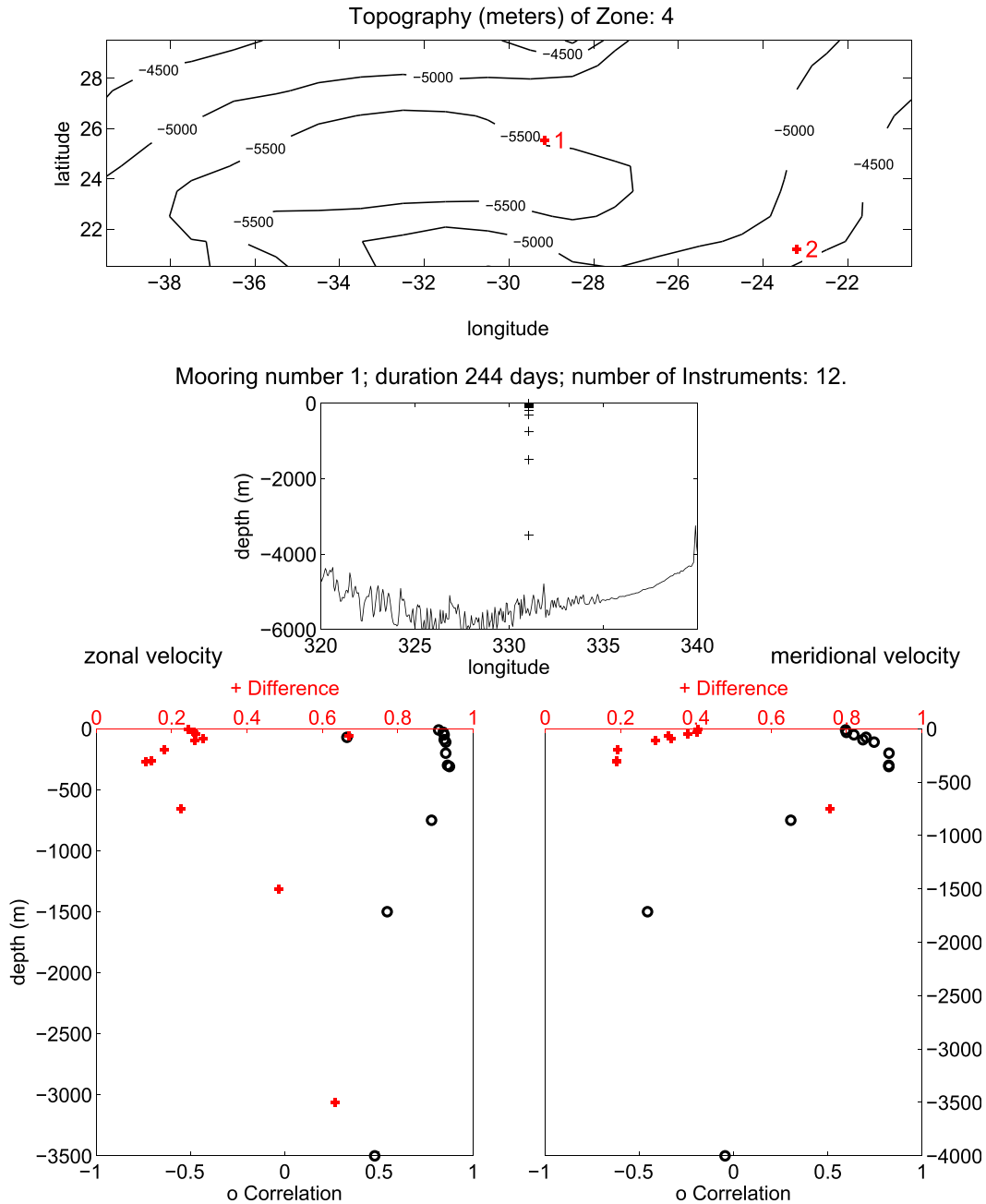zonal velocity   meridional velocity

FIG. 10. (top) Topography of zone 4 with position of each mooring in the zone. (middle) Mooring 1 with zonal topography at the latitude of the mooring and the depth of each instrument. Length of the record is 244 days. (bottom) Correlation between prediction by the model and real data from current meters for the (left) zonal velocity U and the (right) meridional velocity V for mooring 1 at zone 4. Differences calculated with (23) are shown on the same plot (red crosses).

where mean currents have a small intensity. Westward-propagating motions have been reported by a number of studies at this latitude (e.g., Osychny and Cornillon 2004). The topography, shown in Fig. 10, is quite flat. Mooring locations are shown in the same figure. We will only study mooring 1, which is situated at the center of the zone; it has

12 instruments on the vertical from 10-m depth to 3500 m, which gives a good sampling. However, the duration of the record is quite short: 244 days. As a result, all the time scales longer than approximately 100 days cannot be tested.

The altimetry gives a proportion of energy in $\lambda^2 > 0$ compared to the total energy of 54%, which indicates
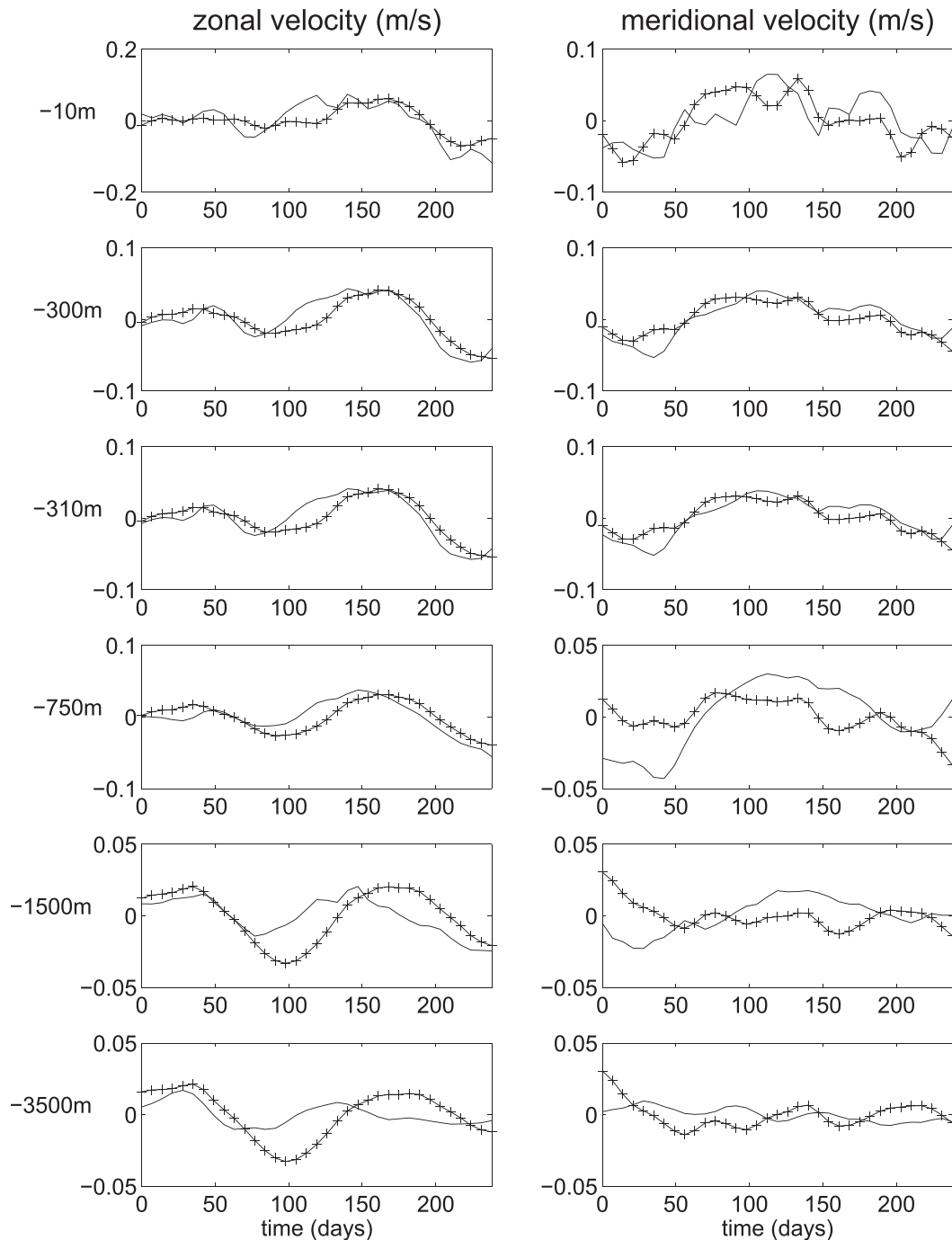
FIG. 11. Zone 4, mooring 1. Time series of the prediction (crosses) and of real data (line) at different depth for (left) zonal velocity and (right) meridional velocity.

a quasi equipartition between forced motion ($\lambda^2 < 0$) and Rossby wave dynamics ($\lambda^2 > 0$). Correlation for the zonal and meridional velocities are shown in Fig. 10. Correlations are larger than 0.8 in the upper 500 m and decrease slowly for the zonal velocity and quite rapidly for the meridional velocity with depth. The correlation

for the meridional velocity is always smaller than for the zonal one. In Fig. 11 the comparison of the time series shows that the prediction follows the current meter observations quite well at −300, −310, and −750 m for the zonal velocity and at −300 m but not so well at the other depths.
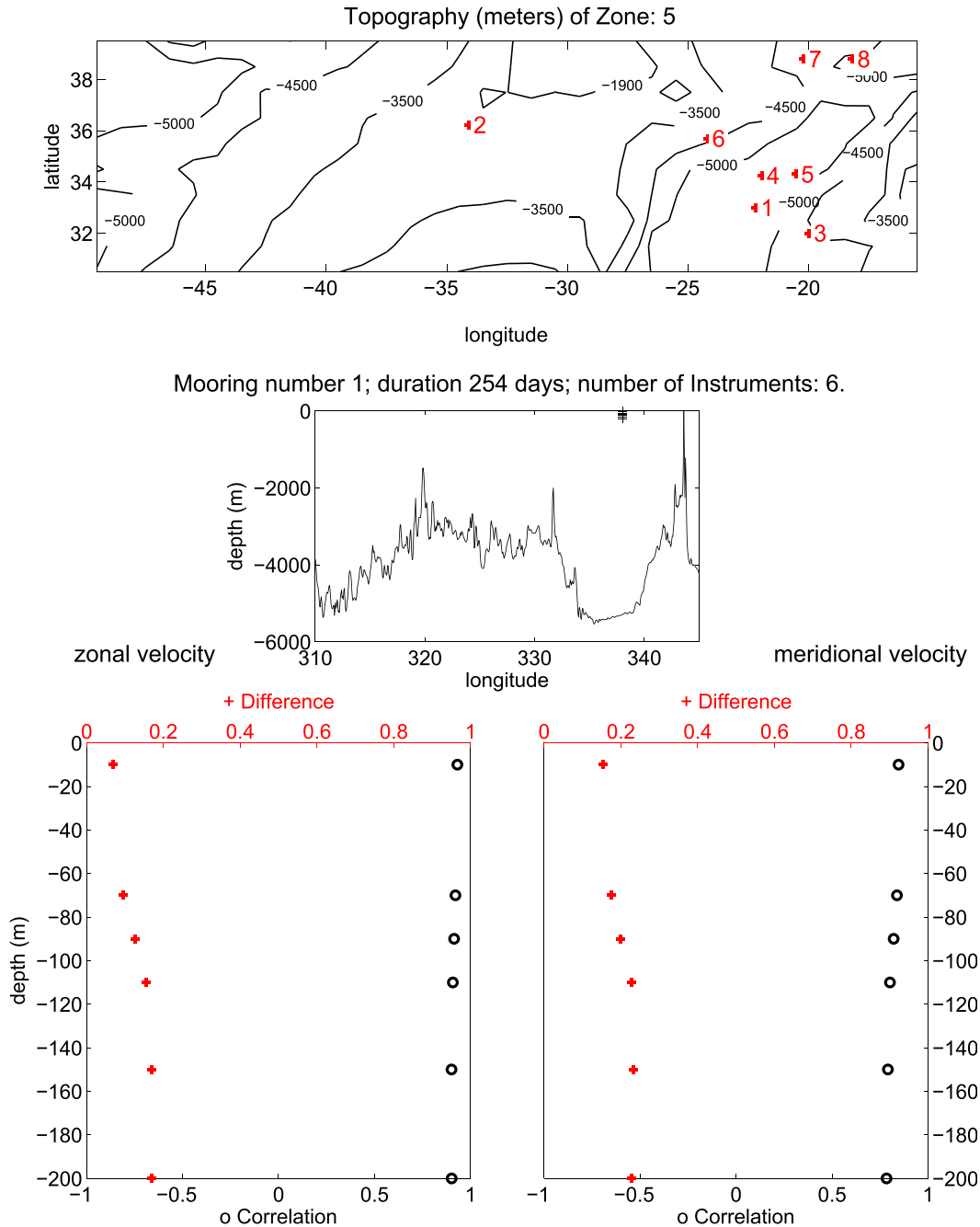
FIG. 12. As in Fig. 10, but for zone 5 with a record length of 254 days.

(ii) Zone 5

Zone 5 is still in the Atlantic Ocean but at a higher latitude than zone 4, and topography is not flat: the Atlantic Ridge crosses the middle of the zone. We thus expect the model to be less accurate here. The altimetry gives a proportion of energy in $\lambda^2 > 0$ compared to the total energy of 49% that, as for zone 4, indicates a quasi equipartition between forced motion ($\lambda^2 < 0$) and Rossby

wave dynamics ($\lambda^2 > 0$). Correlations are shown in Figs. 12, 14, 15, 16, and 18. Mooring 1 has a duration of 254 days, which is again a bit short for our study, and six instruments in the first 200 m. The available data are reasonably well predicted by our model since the correlations for the zonal and meridional velocities are always larger than 0.8. The time series are shown in Fig. 13 and reveal that the large time scales are well predicted but that the small ones (shorter than a month) are badly predicted.
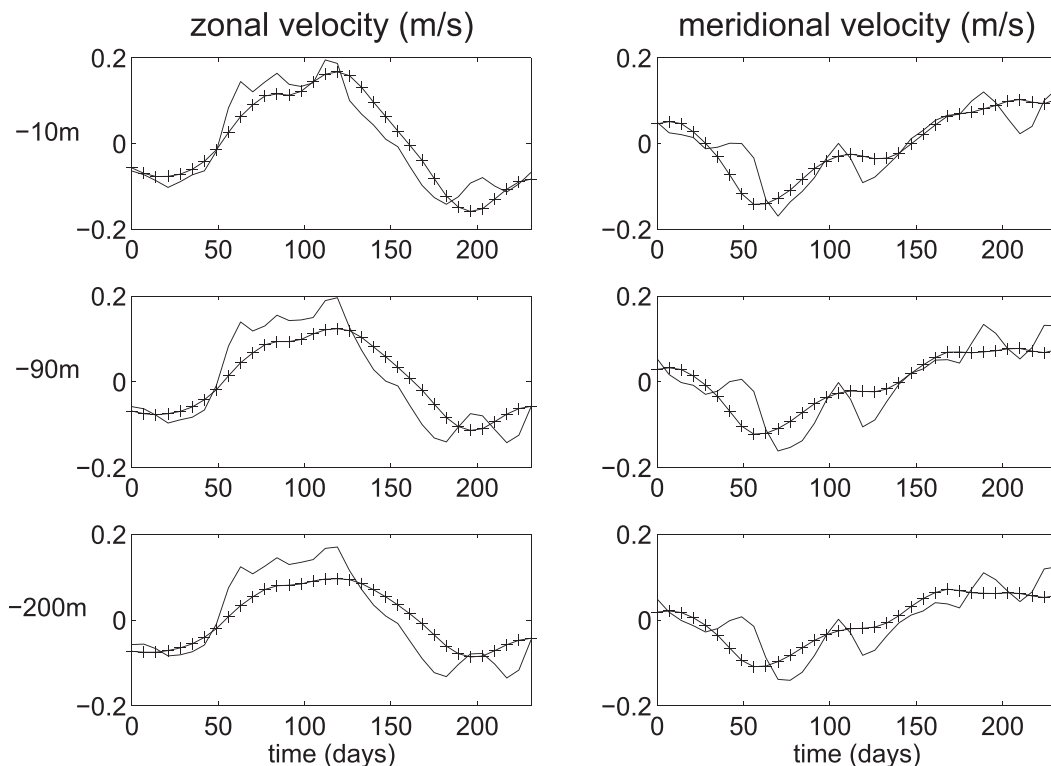
FIG. 13. Zone 5, mooring 1. Time series of the prediction (crosses) and of real data (line) at different depth for (left) zonal velocity and (right) meridional velocity.

Mooring 2 (Fig. 14), which has five instruments just above the Atlantic Ridge, at a depth of approximately 2000 m, outlines the importance of the topography near the sea floor since correlations are close to zero. Mooring 3 is situated in the southeast part of the zone and has three instruments from 500 to 3500 m, the last instrument being very close to the seafloor, recording for a 287-day period. The correlation shown in Fig. 15 is low for the two instruments below 1000 m; it can be explained by the very southern position of the mooring in the zone we chose. Mooring 4 is situated approximately 3° to the northwest of mooring 3 and has three instruments between 500 m and 3500 m withr a recording duration of 292 days. The calculated correlations are shown in Fig. 16 and show that the prediction is accurate for the instruments at 500 and 1000 m. The time series, shown in Fig. 17, show that the large time scales are well predicted for the 500-m current meter but that the prediction is poor for the v component at 3500-m depth. Mooring 5, situated in the eastern part of the zone, has three instruments at 500, 1000, and 3500 m and a recording duration of 291 days. Calculated correlations in Fig. 18 seem to be accurate in the top 1000 m, but the time series (Fig. 19) shows that the variability is poorly predicted for both meridional and zonal velocities, except maybe for the meridional velocity at 500 m.

To conclude this part, although very few current meters are placed in suitable regions to test our model assumptions (low latitudes, weak mean currents, far from lateral boundaries, and long periods), the comparison shows that the method has some skill in reproducing the currents below the surface and in some cases the skill extends to surprisingly deep levels. As expected at higher latitudes and near the boundaries of the basins, the model cannot give accurate results because of the linearity assumptions.

3) PROJECTION ON TRADITIONAL VERTICAL MODES

Our model provides $\psi(x, y, z, t)$ and as a result we can calculate the projection of the depth-integrated kinetic energy on traditional vertical modes that are the solutions of the following equation:

$$\frac{d}{dz}\left[\frac{f_0^2}{N^2(z)}\frac{d\phi}{dz}(z)\right] + \lambda^2\phi(z) = 0, \qquad (24)$$

together with the boundary condition $d\phi/dz = 0$ at $z = 0$ and $z = -H$. We then write $(u, v)(x, y, z, t) = \sum_n (\alpha_n^u, \alpha_n^v)(x, y, t)\phi_n(z)$, so that
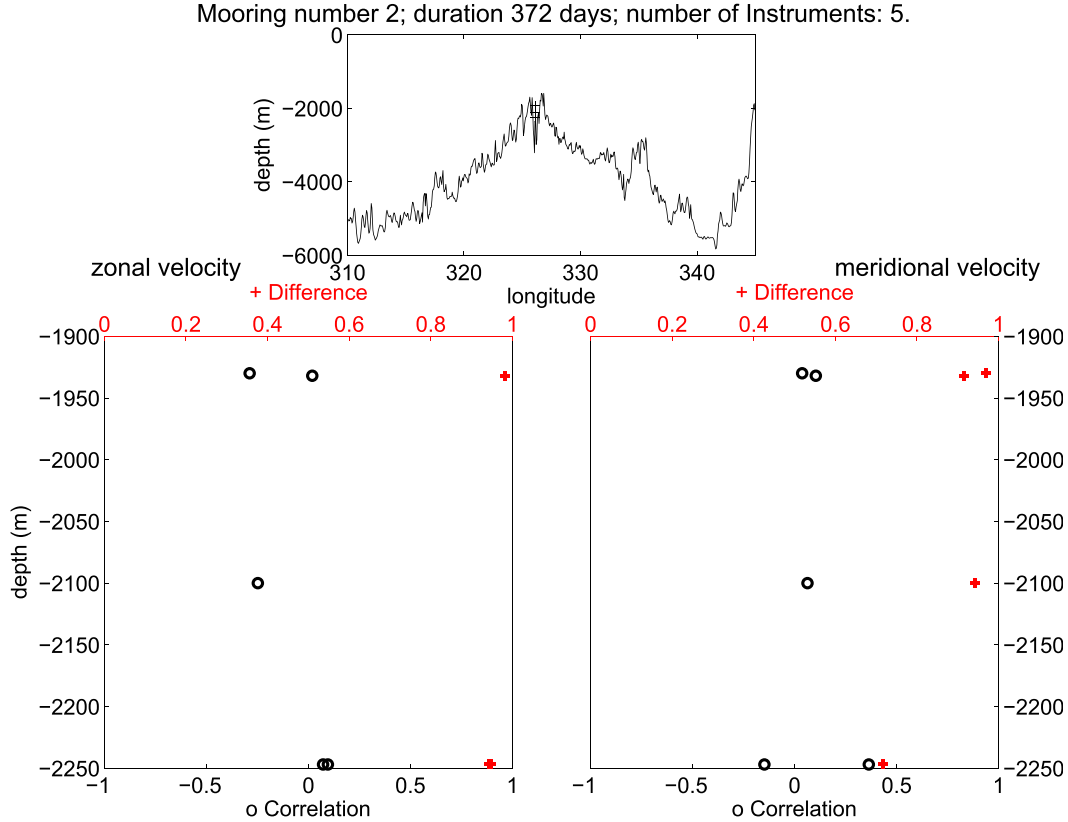
FIG. 14. (top) Mooring 2, zone 5, with zonal topography at the latitude of the mooring and the depth of each instrument. Length of the record is 372 days. (bottom) Correlation between prediction by the model and real data from current meters for (left) zonal velocity U and the (right) meridional velocity V for mooring 2 in zone 5. Differences calculated with (23) are shown on the same plot (red crosses).

$$\overline{\mathrm{KE}_{\mathrm{tot}}^{n}} = 0.5[\overline{(\alpha_n^u)^2} + \overline{(\alpha_n^v)^2}], \qquad (25)$$

where $\mathrm{KE}_{\mathrm{tot}}^{n}$ is the kinetic energy in mode n. We have used the orthogonality property of ϕ_n; $\int_{-H}^{0} \phi_i(z)\phi_j(z)\,dz = \delta_{ij}H$ and the bar indicates the spatial and temporal mean. We perform the calculation in three regions (A, B, and C) of equal size situated in the Atlantic and Pacific Oceans (see Fig. 8) centered at 22.5°N, where we believe our model gives accurate results. Then we average the results for the three zones and obtain a kinetic energy distribution of 68%, 25%, and 5% for the barotropic and first two baroclinic modes. The calculation is also performed at different latitudes and reveals that latitude variation influences the proportion of the total energy in each mode. Indeed, the percentage of energy in the barotropic mode increases from 53% at −10°S to 82% at −15°S in the South Atlantic and decreases in the first baroclinic mode from 31% to 16%. The same variation is obtained in the North Atlantic. This result is in agreement with a study of Ollitrault and Colin de Verdière (2014), who report evidence based on comparisons of eddy kinetic energy at the

surface from satellite altimetry and at 1000 m from Argo float displacements that anomalies are more barotropic at higher latitudes. A dynamical interpretation of these phenomena might be given by LaCasce and Pedlosky (2004), who suggested that baroclinic Rossby waves are vulnerable to baroclinic instability and eventually become barotropic. This effect is likely to be stronger when the latitude increases since the baroclinic waves are slower and thus are more likely influenced by baroclinic instability.

4) EXCITATION OF OCEANIC FREE MODES:
   LATITUDE VARIATION

There is considerable interest in identifying the presence of free waves (the waves that satisfy $\partial \psi / \partial z = 0$ at $z = 0$ and $z = -H$) in the altimeter data in order to evaluate the traditional linear theory of Rossby waves (with no mean flow and no topography). To decide if a wavenumber frequency combination (k, l, ω) belongs to a free wave or not, the proximity to the free Rossby wave dispersion relation of a given vertical mode has to
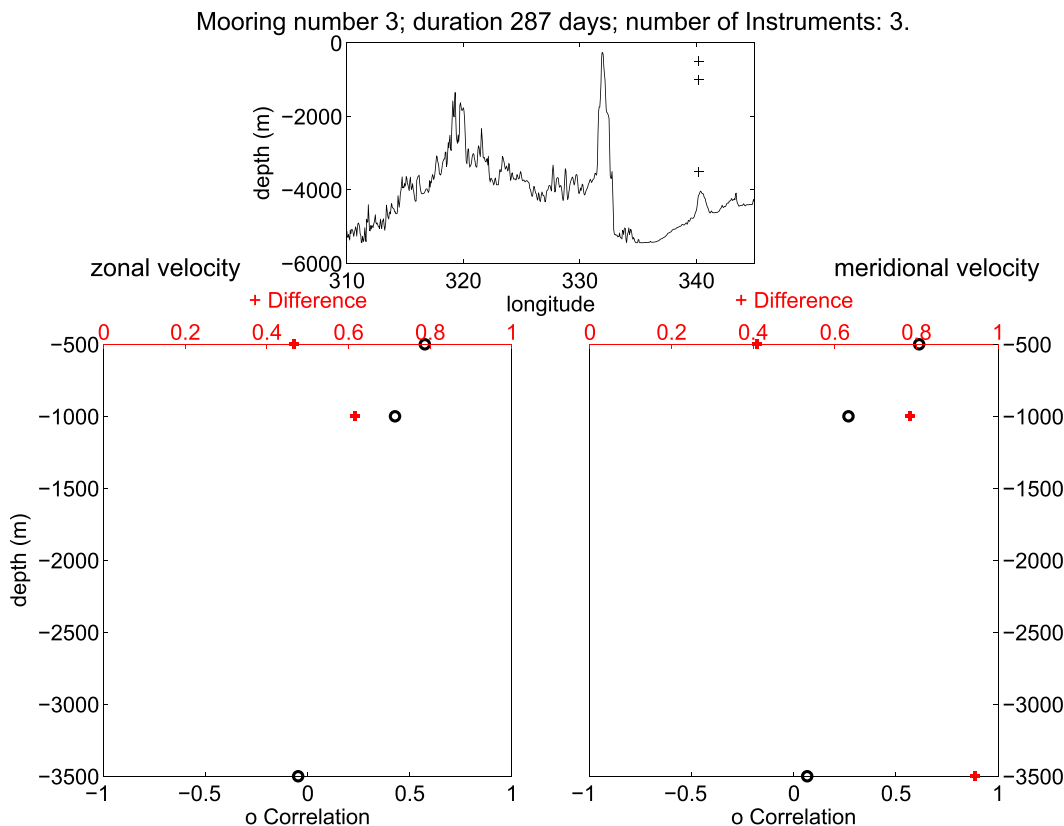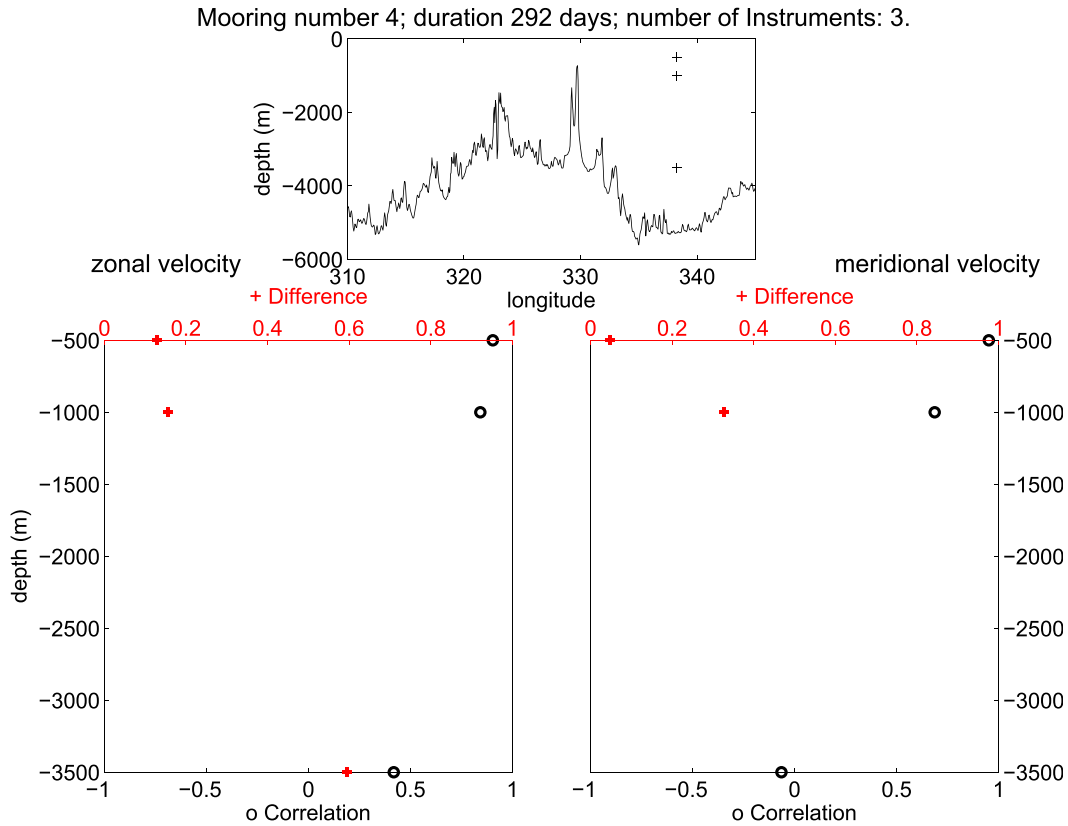
FIG. 15. As in Fig. 14, but for mooring 3 with a record length of 287 days.

be measured. To do so, a tolerance coefficient ϵ is defined so that the kinetic energy $KE(k, l, \omega)$ is attributed to mode i if $\lambda_i - \epsilon < \lambda < \lambda_i + \epsilon$, where $\lambda^2 = -(k^2 + l^2) + [(\beta k)/\omega]$, λ_i is the deformation radius of mode i, and ϵ is a small coefficient. However, in practice, we only calculate the barotropic and first baroclinic modes since all others represent only a very small fraction of the total energy ($<1\%$). We perform the calculation in the North Atlantic and North Pacific for different latitudes. Results are shown in Fig. 20 and outline the relatively small percentage (20%) of energy contained in free modes. This observation outlines that our method for calculating the vertical structure is sensible since it allows the energy to lie outside the traditional dispersion relation. In the Pacific Ocean, the energy in barotropic free mode is constant over latitude. In the Atlantic, it remains constant (10%) below latitude 25°N and then increases to reach 16% at 32°N. The energy in the baroclinic free mode increases slowly with latitude in the Pacific. In the Atlantic, it increases below latitude 25° and decreases afterward. Timescales ($T = 2\pi/\omega$) and length scales ($L = 2\pi/\sqrt{k^2 + l^2}$) of the maximum of energy in each free mode are indicated in Table 2. In the Pacific it shows that the maximum of energy in the barotropic free mode

has similar length scale and time scale over latitude, whereas the time scale of baroclinic free modes increases with latitude. In the Atlantic the length scale remains similar over latitude for both modes (around 500 km) and the time scale is larger at 25°N (1000 days) than at 20° and 30°N (500 days). No significant difference has been found between barotropic and baroclinic free modes in the Atlantic. Since meridional wavelengths are much shorter than zonal ones, these free waves transport energy westward.
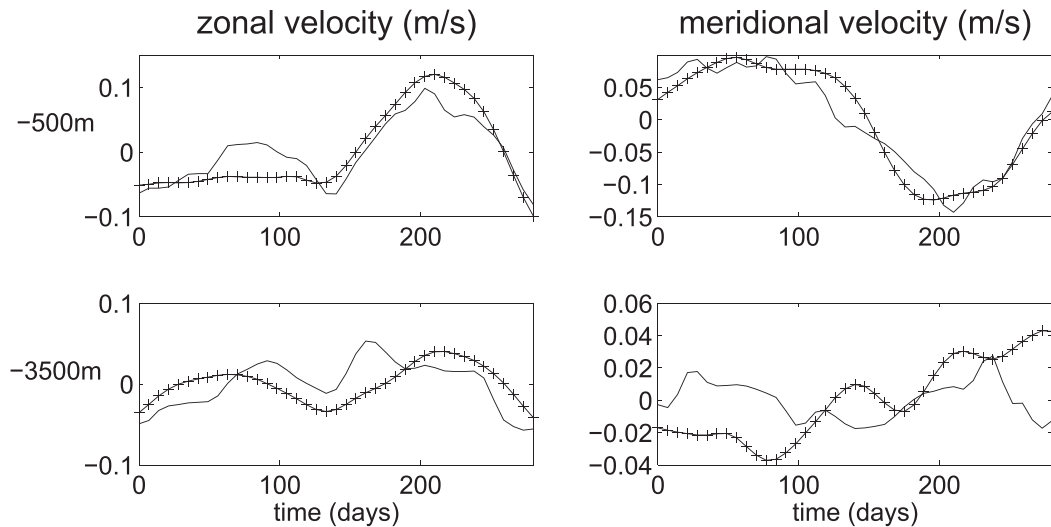
4. Summary and discussion

The vertical structure of Rossby waves has been studied here with a linear model based on the quasigeostrophic equations. In the first part of the study, we showed how it is possible to solve the linear quasigeostrophic equations to predict the vertical structure of the waves. The method consists of selecting a rectangular zone where we perform a Fourier analysis of sea surface height to obtain all the frequencies and wavenumbers (k, l, ω). The vertical structure is then calculated for each (k, l, ω) and reconstructed in the physical space. The main difficulty of the method was removing the

Mooring number 4; duration 292 days; number of Instruments: 3.

FIG. 16. As in Fig. 14, but for mooring 4 with a record length of 292 days.

resonance of spurious modes (excitation of the free modes). We removed them using the condition $\partial\psi/\partial z = 0$ at the surface, thus assuming no forcing waves. This assumption may seem awkward since some studies (e.g., White 1977; Hill et al. 2000) show that Rossby waves can

be detected in surface temperature data. A recent study by O'Brien et al. (2013) suggests that the density anomalies are formed by horizontal advection of the background density fields by the geostrophic velocities induced by the waves rather than the result of a vertical

FIG. 17. Zone 5, mooring 4. Time series of the prediction (crosses) and of real data (line) at different depths for (left) zonal and (right) meridional velocity.

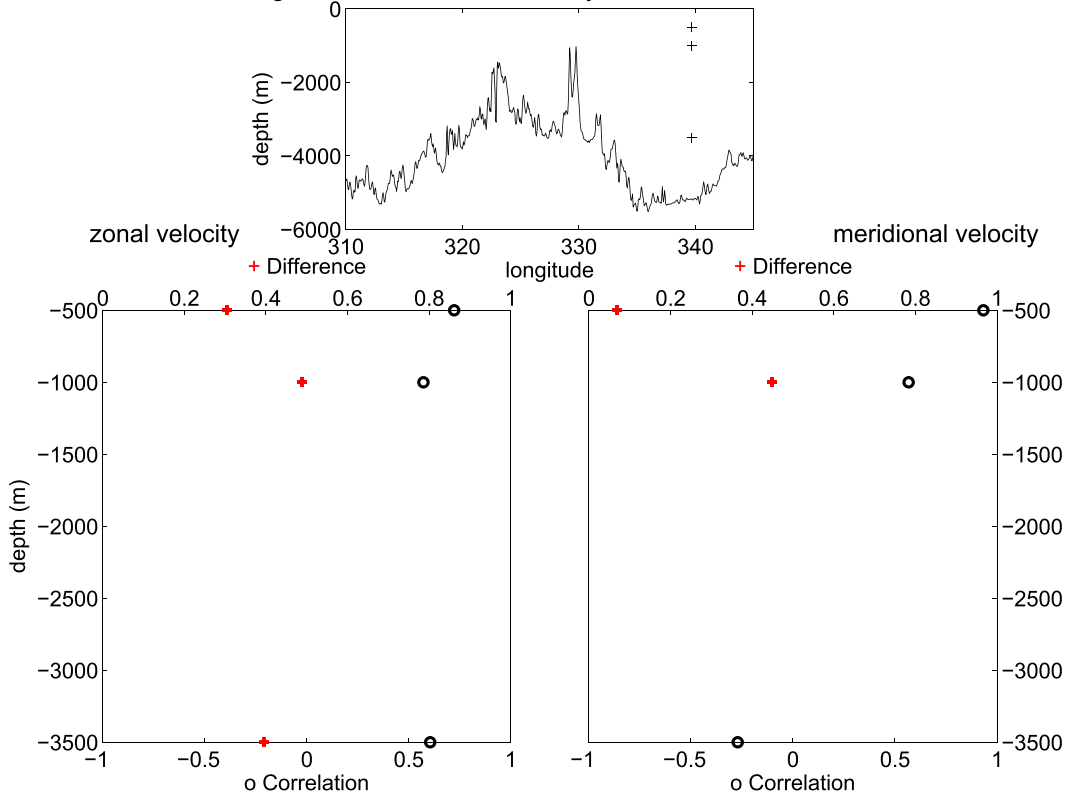Mooring number 5; duration 291 days; number of Instruments: 3.

FIG. 18. As in Fig. 14, but for mooring 5 with a record length of 292 days.

mechanism. However, our assumption of the zero density anomaly at the surface holds as long as these effects due to the interaction of the Rossby wave with the mean flow are small. The mean flow effect on the surface boundary condition can be seen in the following equation:

$$\partial_t \psi'_z + J(\overline{\psi}, \psi'_z) + J(\psi', \overline{\psi_z}) = 0, \qquad (26)$$

where the bar is the time mean. The first term of this equation dominates the second if the time scale is shorter than the advective scale and dominates the third if the nondimensional number $(\beta R_d^2)/[H_{bc}(U/H_{mean})] \gg 1$ [this
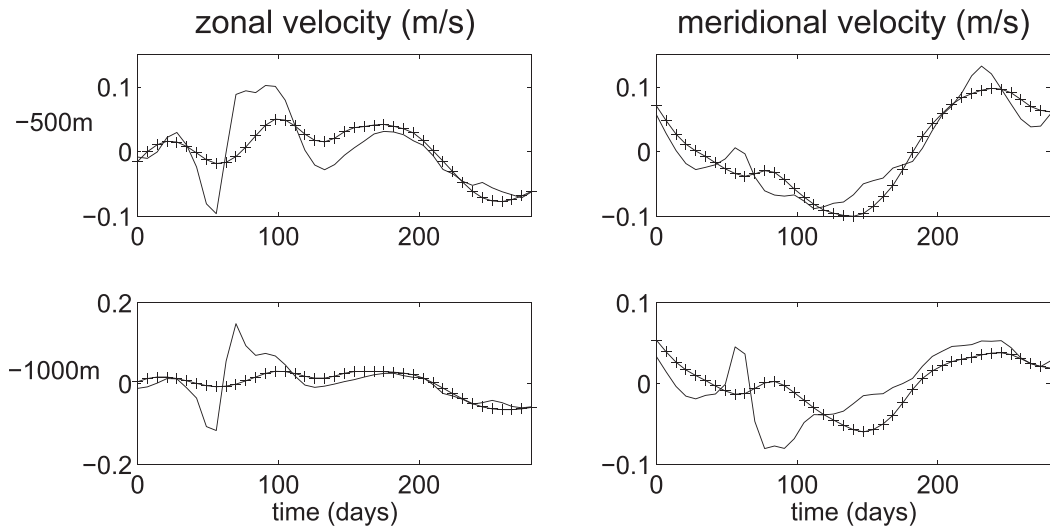

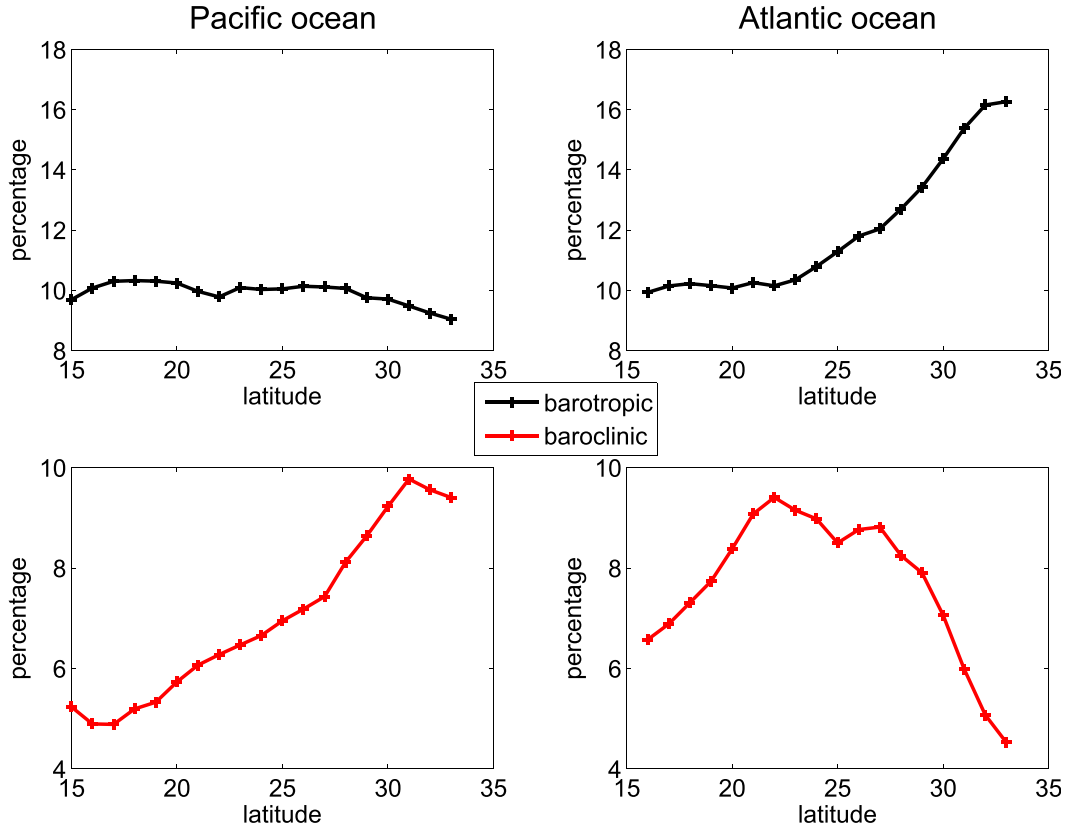FIG. 19. As in Fig. 17, but for mooring 5. Zone 5, mooring 5.

FIG. 20. Percentage of energy that can be attributed to the (top) barotropic and to the (bottom) first baroclinic mode as a function of latitude. (left) Pacific Ocean (170° to 220°); (right) Atlantic Ocean (290° to 340°).

number is obtained by assuming a long first baroclinic Rossby wave in (26); R_d is the deformation radius, H_{bc} is the vertical scale of the wave, U is the order of magnitude of the mean flow velocity, and H_{mean} is its vertical scale]. For example, at low latitude $\beta \sim 2.10^{-11}\,\mathrm{s}^{-1}\,\mathrm{m}^{-1}$, $R_d \sim 100\,\mathrm{km}$, $H_{\mathrm{bc}} \sim 1000\,\mathrm{m}$, $U \sim 0.01\,\mathrm{m\,s}^{-1}$, and $H_{\mathrm{mean}} \sim 1000\,\mathrm{m}$ gives $(\beta R_d^2)/[H_{\mathrm{bc}}(U/H_{\mathrm{mean}})] \sim 20$. According to this nondimensional number, the effect of the advection of mean density by the wave-induced velocities is larger at high latitudes and can be neglected at low latitudes.

We first tested the model with a primitive equation simulation of a wind-driven double gyre. Results showed that the model gives accurate predictions at low latitude between 10° and 30° and when nonlinearities are weak. This can be explained by the decreasing of baroclinic Rossby wave phase speed with latitude and as a result the increasing role of nonlinearities.

We then compared the model predictions with real data (altimetry from AVISO and current meters data) and showed that the model can reproduce oceanic currents below the surface. We then showed that the model gives a vertical partition of energy on traditional vertical

modes of approximately 68%, 25%, and 5% in the barotropic mode and two first baroclinic modes and that this partition becomes more barotropic with increasing latitude. Wunsch (1997) found an energy partition of approximately 45% and 45% in, respectively, the

TABLE 2. Zonal scale (km), meridional scale (km), and time scales (days) estimated from the maximum of energy contained in the barotropic (BT) and first baroclinic (BC) free modes. Different latitudes for the North Atlantic and North Pacific are shown.

Atlantic latitude	Time scale		Zonal scale		Meridional scale	
	BT	BC	BT	BC	BT	BC
20	500	500	5000	2000	600	600
25	1000	600	5000	2000	400	400
30	500	500	1200	800	600	600

Pacific latitude	Time scale		Zonal scale		Meridional scale	
	BT	BC	BT	BC	BT	BC
20	250	250	2000	1000	400	600
25	500	1000	4000	4000	600	600
30	500	2000	4000	4000	400	600

barotropic and first baroclinic modes and the differences with our results can be explained by the following:

- Our study focus on regions of relatively low latitude ($<30°$N or S), far from all boundaries. Most of the current meters used in Wunsch (1997) are situated at latitudes larger than $30°$N or S (65%). We may expect to find different dynamics at high and low latitudes.
- Time scales in Wunsch (1997) range from 2 days (inverse of Nyquist frequency) to several weeks, whereas in our study, time scales ranges from two weeks to several years. The energy proportion in vertical modes might depend upon the choice of time scales.
- In our study, the projection of our results is made on traditional vertical modes (for which $\partial\psi/\partial z(z=0)=0$) so that our method can be compared with previous studies. But the vertical structure calculated here does not assume zero vertical velocity at the surface and thus might not be well represented by the traditional vertical modes. Smith and Vanneste (2013) found a basis that might solve this problem.

The main novelty of the present method is to "read" the vertical structure of pressure anomalies in their horizontal and time surface field. In Scott and Furnival (2012), the vertical structure was independent of the surface field properties leading to low prediction under 600 m. The second novelty presented in this paper is the use of real data (AVISO and current meters) in order to test our model.

Since some authors have emphasized the discrepancy between first baroclinic mode theoretical and observational phase speed of Rossby waves, the question of the validity of the linear equations that describe the waves is frequently questioned in the literature (starting from Killworth et al. 1997). Here, the approach is different. The phase speed is read in the altimetric data, and the vertical structure is predicted. In regions where our model works well, the structure is more barotropic than the first baroclinic mode assumption of Chelton and Schlax (1996). In most of the studies about Rossby waves, the meridional wavenumber is also assumed to be zero (e.g., in Chelton and Schlax 1996 or Osychny and Cornillon 2004), which might not be accurate since anomalies in the zone that we studied have more or less the same zonal and meridional size. Therefore, we chose to use rectangular boxes to perform the Fourier analysis rather than lines of constant latitude that cannot account for meridional variations. We found that only a small fraction of kinetic energy (20%) can be attributed to free waves in the Pacific and Atlantic Oceans. The period of the waves is between 500 and 1000 days with wavelengths between 250 and 2000 km, values that are similar for the barotropic and baroclinic Rossby waves.

This result, which is similar to the result of Wunsch (2010) that the energy lays along a "nondispersive line," raises the question of the dynamics behind this energy distribution. Forced waves could be an answer, but the spurious mode of (6) shows that the forcing would have to be very strong to produce waves detectable in the SSH with wavelength and frequency far from the dispersion relationship of the free modes. Another mechanism could be the modification of the waves by constant mean flow or topography as studied by Killworth's articles (Killworth et al. 1997 and Killworth and Blundell 1999, 2003a), but dimensional analysis (see Colin de Verdière and Tailleux 2005) and our results show that this mechanism should not be important at low latitude, where a substantial part of the energy clearly does not belong to the free modes.

This model could be improved in several ways. The first improvement would be to break the spatial periodicity hypothesis that we made to perform the calculation with a 3D Fourier transform. Breaking the 2D horizontal periodicity would allow us to remove the errors near the boundaries of the zone and perform a global calculation of the anomalies' vertical structure. To do this, one would have to calculate the horizontal eigenmodes for the whole oceanic basin and project the SSH on these modes. Then, the second improvement would be to add the effect of a mean flow on the anomalies. Indeed, it is expected that this effect has a significant importance for latitudes higher than $30°$.

REFERENCES

Anderson, D. L., and A. Gill, 1975: Spin-up of a stratified ocean, with applications to upwelling. *Deep-Sea Res. Oceanogr. Abstr.,* **22,** 583–596, doi:10.1016/0011-7471(75)90046-7.

Andrews, D. G., J. R. Holton, and C. B. Leovy, 1987: *Middle Atmosphere Dynamics.* Academic Press, 489 pp.

Bleck, R., and D. Boudra, 1986: Wind-driven spin-up in eddy-resolving ocean models formulated in isopycnic and isobaric coordinates. *J. Geophys. Res.,* **91,** 7611–7621, doi:10.1029/JC091iC06p07611.

Chelton, D. B., and M. G. Schlax, 1996: Global observations of oceanic Rossby waves. *Science,* **272,** 234–238, doi:10.1126/science.272.5259.234.

Colin de Verdière, A., and R. Tailleux, 2005: The interaction of a baroclinic mean flow with long Rossby waves. *J. Phys. Oceanogr.,* **35,** 865–879, doi:10.1175/JPO2712.1.

Gill, A. E., 1982: *Atmosphere–Ocean Dynamics.* Academic Press, 662 pp.

Grimshaw, R., and J. S. Allen, 1988: Low-frequency baroclinic waves off coastal boundaries. *J. Phys. Oceanogr.,* **18,** 1124–1143, doi:10.1175/1520-0485(1988)018<1124:LFBWOC>2.0.CO;2.

Hill, K. L., I. S. Robinson, and P. Cipollini, 2000: Propagation characteristics of extratropical planetary waves observed in the ATSR global sea surface temperature record. *J. Geophys. Res.,* **105,** 21 927–21 945, doi:10.1029/2000JC900067.

Hirschi, J. J., P. D. Killworth, J. R. Blundell, and D. Cromwell, 2009: Sea surface height signals as indicators for oceanic meridional mass transports. *J. Phys. Oceanogr.,* **39,** 581–601, doi:10.1175/2008JPO3923.1.

Holland, W. R., and P. B. Rhines, 1980: An example of eddy-induced ocean circulation. *J. Phys. Oceanogr.,* **10,** 1010–1031, doi:10.1175/1520-0485(1980)010<1010:AEOEIO>2.0.CO;2.

Isern-Fontanet, J., G. Lapeyre, P. Klein, B. Chapron, and M. W. Hecht, 2008: Three-dimensional reconstruction of oceanic mesoscale currents from surface information. *J. Geophys. Res.,* **113,** C09005, doi:10.1029/2007JC004692.

Jacobs, G., H. Hurlburt, J. Kindle, E. Metzger, J. Mitchell, W. Teague, and A. Wallcraft, 1994: Decade-scale trans-Pacific propagation and warming effects of an El Niño anomaly. *Nature,* **370,** 360–363, doi:10.1038/370360a0.

Killworth, P. D., and J. R. Blundell, 1999: The effect of bottom topography on the speed of long extratropical planetary waves. *J. Phys. Oceanogr.,* **29,** 2689–2710, doi:10.1175/1520-0485(1999)029<2689:TEOBTO>2.0.CO;2.

——, and ——, 2003a: Long extratropical planetary wave propagation in the presence of slowly varying mean flow and bottom topography. Part I: The local problem. *J. Phys. Oceanogr.,* **33,** 784–801, doi:10.1175/1520-0485(2003)33<784:LEPWPI>2.0.CO;2.

——, and ——, 2003b: Long extratropical planetary wave propagation in the presence of slowly varying mean flow and bottom topography. Part II: Ray propagation and comparison with observations. *J. Phys. Oceanogr.,* **33,** 802–821, doi:10.1175/1520-0485(2003)33<802:LEPWPI>2.0.CO;2.

——, D. B. Chelton, and R. A. de Szoeke, 1997: The speed of observed and theoretical long extratropical planetary waves. *J. Phys. Oceanogr.,* **27,** 1946–1966, doi:10.1175/1520-0485(1997)027<1946:TSOOAT>2.0.CO;2.

LaCasce, J., and J. Pedlosky, 2004: The instability of Rossby basin modes and the oceanic eddy field. *J. Phys. Oceanogr.,* **34,** 2027–2041, doi:10.1175/1520-0485(2004)034<2027:TIORBM>2.0.CO;2.

Lapeyre, G., 2009: What vertical mode does the altimeter reflect? On the decomposition in baroclinic modes and on a surface-trapped mode. *J. Phys. Oceanogr.,* **39,** 2857–2874, doi:10.1175/2009JPO3968.1.

——, and P. Klein, 2006: Dynamics of the upper oceanic layers in terms of surface quasigeostrophy theory. *J. Phys. Oceanogr.,* **36,** 165–176, doi:10.1175/JPO2840.1.

Matsuno, T., 1970: Vertical propagation of stationary planetary waves in the winter Northern Hemisphere. *J. Atmos. Sci.,* **27,** 871–883, doi:10.1175/1520-0469(1970)027<0871:VPOSPW>2.0.CO;2.

Milliff, R. F., and J. C. McWilliams, 1994: The evolution of boundary pressure in ocean basins. *J. Phys. Oceanogr.,* **24,** 1317–1338, doi:10.1175/1520-0485(1994)024<1317:TEOBPI>2.0.CO;2.

O'Brien, R. C., P. Cipollini, and J. R. Blundell, 2013: Manifestation of oceanic Rossby waves in long-term multiparametric satellite datasets. *Remote Sens. Environ.,* **129,** 111–121, doi:10.1016/j.rse.2012.10.024.

Ollitrault, M., and A. Colin de Verdière, 2014: The ocean general circulation near 1000-m depth. *J. Phys. Oceanogr.,* **44,** 384–409, doi:10.1175/JPO-D-13-030.1.

Osychny, V., and P. Cornillon, 2004: Properties of Rossby waves in the North Atlantic estimated from satellite data. *J. Phys. Oceanogr.,* **34,** 61–76, doi:10.1175/1520-0485(2004)034<0061:PORWIT>2.0.CO;2.

Pedlosky, J., 1987: *Geophysical Fluid Dynamics.* 2nd ed. Springer-Verlag, 710 pp.

Philander, S., 1978: Forced oceanic waves. *Rev. Geophys.,* **16,** 15–46, doi:10.1029/RG016i001p00015.

Qiu, B., and S. Chen, 2005: Variability of the Kuroshio Extension jet, recirculation gyre, and mesoscale eddies on decadal time scales. *J. Phys. Oceanogr.,* **35,** 2090–2103, doi:10.1175/JPO2807.1.

Scott, R. B., and D. G. Furnival, 2012: Assessment of traditional and new eigenfunction bases applied to extrapolation of surface geostrophic current time series to below the surface in an idealized primitive equation simulation. *J. Phys. Oceanogr.,* **42,** 165–178, doi:10.1175/2011JPO4523.1.

Smith, K. S., and J. Vanneste, 2013: A surface-aware projection basis for quasigeostrophic flow. *J. Phys. Oceanogr.,* **43,** 548–562, doi:10.1175/JPO-D-12-0107.1.

Tailleux, R., and J. C. McWilliams, 2000: Acceleration, creation, and depletion of wind-driven, baroclinic Rossby waves over an ocean ridge. *J. Phys. Oceanogr.,* **30,** 2186–2213, doi:10.1175/1520-0485(2000)030<2186:ACADOW>2.0.CO;2.

——, and ——, 2001: The effect of bottom pressure decoupling on the speed of extratropical, baroclinic Rossby waves. *J. Phys. Oceanogr.,* **31,** 1461–1476, doi:10.1175/1520-0485(2001)031<1461:TEOBPD>2.0.CO;2.

Tulloch, R., J. Marshall, and K. S. Smith, 2009: Interpretation of the propagation of surface altimetric observations in terms of planetary waves and geostrophic turbulence. *J. Geophys. Res.,* **114,** C02005, doi:10.1029/2008JC005055.

Wang, J., G. R. Flierl, J. H. LaCasce, J. L. McClean, and A. Mahadevan, 2013: Reconstructing the ocean's interior from surface data. *J. Phys. Oceanogr.,* **43,** 1611–1626, doi:10.1175/JPO-D-12-0204.1.

White, W. B., 1977: Annual forcing of baroclinic long waves in the tropical North Pacific Ocean. *J. Phys. Oceanogr.,* **7,** 50–61, doi:10.1175/1520-0485(1977)007<0050:AFOBLW>2.0.CO;2.

Wright, C. J., R. B. Scott, D. Furnival, P. Ailliot, and F. Vermet, 2013: Global observations of ocean-bottom subinertial current dissipation. *J. Phys. Oceanogr.,* **43,** 402–417, doi:10.1175/JPO-D-12-082.1.

Wunsch, C., 1997: The vertical partition of oceanic horizontal kinetic energy. *J. Phys. Oceanogr.,* **27,** 1770–1794, doi:10.1175/1520-0485(1997)027<1770:TVPOOH>2.0.CO;2.

——, 2010: Toward a midlatitude ocean frequency–wavenumber spectral density and trend determination. *J. Phys. Oceanogr.,* **40,** 2264–2281, doi:10.1175/2010JPO4376.1.

Zang, X., and C. Wunsch, 1999: The observed dispersion relationship for North Pacific Rossby wave motions. *J. Phys. Oceanogr.,* **29,** 2183–2190, doi:10.1175/1520-0485(1999)029<2183:TODRFN>2.0.CO;2.